Bi-stability of the Filchner-Ronne Ice Shelf Cavity Circulation and Basal Melt

Julia E. Hazel[1], **Andrew L. Stewart**[1]

[1]University of California Los Angeles, Department of Atmospheric and Oceanic Sciences Math Sciences Building, 520 Portola Plaza, Los Angeles, CA 90095

Key Points:

- The Filchner-Ronne Ice Shelf cavity supports bi-stable warm and cold states under identical atmospheric forcing in a regional model
- The Filchner-Ronne Ice Shelf cavity is flooded by the denser of HSSW (cold) or CDW (warm), which in turn sets the melt rate
- Modest changes in offshore winds can switch between cold and warm states by modifying the density of High Salinity Shelf Water

Corresponding author: Julia E. Hazel, jhazel@atmos.ucla.edu

Abstract

Circulation and water mass transformation within the Filchner-Ronne Ice Shelf (FRIS) cavity create precursors to Antarctic bottom water, which closes the global overturning circulation. This water mass transformation is contingent upon a relative low rate of FRIS basal melt, currently around 100–200 Gt/yr. Previous studies have indicated that Antarctic climate changes may induce intrusions of warm modified Warm Deep Water (mWDW) and an order-of-magnitude increase in basal melt, and signatures of mWDW have recently been observed along the face of the FRIS. However, it remains unclear how changes in near-Antarctic climate translate mechanistically to changes in mWDW access to the FRIS cavity.

In this study a regional model is developed to investigate FRIS circulation dependence on local atmospheric state. Experiments with modified initial cavity conditions but identical atmospheric states yield bi-stable "warm" and "cold" FRIS cavity states, with an order-of-magnitude difference in basal melt rates. Idealized atmospheric perturbation experiments reveal that relatively modest perturbations to the katabatic winds shift the FRIS cavity between "warm" and "cold" states, which occur when the FRIS cavity is filled by mWDW or High Salinity Shelf Water (HSSW), respectively. The authors present a conceptual model in which the FRIS cavity state is determined by whether mWDW or HSSW is denser, and thus floods the cavity; these states are bi-stable because the basal melt rate feeds back on the salinity of HSSW. These findings highlight a key role for the katabatic winds in mediating the melt of the FRIS and other Antarctic ice shelves.

1 Introduction

The Filchner-Ronne Ice Shelf (FRIS) in the southern Weddell Sea is Antarctica's largest floating glacier by volume (Moholdt et al., 2014), spanning an area of approximately 450,000km^2 (Fox et al., 1994). Circulation within and adjacent to the FRIS cavity is essential to the closure of the global overturning circulation: polynya formation and ensuing ice production on the continental shelf lead to brine rejection and the formation of High Salinity Shelf Water (HSSW) (Nicholls et al., 2009; Haid & Timmermann, 2013). Dense HSSW accesses the FRIS cavity and recirculates to transform into cold, dense Ice Shelf Water (ISW), which in turn flows northward in the Filchner Depression and escapes as a gravity-driven flow over the sill (Foldvik et al., 2004). As it descends, the overflow water entrains Warm Deep Water (WDW) and circulates in the Weddell Gyre as Weddell Sea Deep/Bottom Waters (WSDW/WSBW) (Gordon et al., 2010). These waters ultimately contribute around 8 Sv to the 10–20 Sv of Antarctic Bottom Water flowing in the abyssal cell of the global overturning circulation (Jullion et al., 2014; Vernet et al., 2019).

The FRIS currently exhibits a relatively low basal melt rate, for example compared to ice shelves that are flooded by relatively warm Circumpolar Deep Water (WDW) (Rignot et al., 2013; Moholdt et al., 2014). While WDW does access the southern Weddell Sea continental shelf, it is primarily present in a colder, modified form (mWDW) due to mixing with Antarctic surface waters (Nicholls et al., 2009). The mWDW is carried onto the continental shelf via a boundary current along the eastern side of the Filchner trough, and has been observed to reach the mouth of the FRIS cavity (Nicholls et al., 2009; Darelius et al., 2016). The reservoir of mWDW on the continental shelf is determined by various processes occurring in the Antarctic Slope Front (ASF): inertial overshoots (Klinck & Dinniman, 2010), thermocline responses to wind stress and surface hydrographic properties (Hattermann et al., 2014; A. L. Stewart & Thompson, 2012), tidal fluctuations (Wang et al., 2013; A. L. Stewart et al., 2018), mesoscale eddies (A. L. Stewart & Thompson, 2013, 2015a), and the interaction of the Antarctic Slope Current (ASC) with bottom topography and troughs that cross-cut the shelf break (St-Laurent et al., 2013; Daae et al., 2017).

If mWDW were to flood the FRIS cavity, it may be expected to substantially increase the basal melt rate, as is characteristic of a switch from "mode 1" (HSSW-driven) to "mode

2" (WDW/CDW-driven) melt (Jacobs et al., 1992; Dinniman et al., 2016). Some model simulations forced by projected future atmospheric states suggest that this may occur during the 21st Century, leading to an order-of-magnitude increase in the FRIS' basal melt rate and a shutdown of dense shelf water production (Hellmer et al., 2012; Thoma et al., 2015). Furthermore, a recent study by Hellmer et al. (2017) suggests that the transition to an mWDW-flooded cavity represents "tipping point": once the cavity had been flooded by mWDW, returning to a present-day atmospheric state did not reverse the changes in the FRIS circulation and melt rate. Rather, Hellmer et al. (2017) found that the FRIS cavity had to be artificially restored to cooler temperatures to return it to its present-day state. This raises the possibility that the FRIS cavity supports multiple stable states, but the relation of these states to processes occurring outside the cavity, such as changes in the atmospheric temperature and circulation, have not yet been explored.

In this study, we investigate the role of the atmospheric state and circulation over the southern Weddell Sea in driving changes in the basal melt rate of the FRIS, with a particular emphasis on abrupt transitions between low-melt and high-melt states. In §2.1 we develop a new regional model configuration for the southern Weddell Sea and the FRIS cavity, and in §2.2 we evaluate the simulated ocean/sea ice state against previous observations. In §3.1 we ascertain that the simulated FRIS cavity circulation is bi-stable: given identical atmospheric and oceanic boundary conditions, the model may equilibrate to either a warm (high-melt) or cold (low-melt) state depending on the initial conditions within the cavity. In §3.2 we then perform idealized atmospheric perturbation experiments, and show that changes in the offshore winds are particularly efficient in forcing a "switch" between the warm and cold FRIS cavity states. In §4.1 we perform a suite of perturbation experiments to map out a hysteresis loop for the cavity state as the meridional wind strength is varied, and examine how the cavity properties vary as the FRIS transitions between warm and cold states. In §4.2 we elucidate our findings via a conceptual model of the FRIS cavity circulation in which transitions between warm and cold states are dictated by the denser of mWDW or HSSW flooding the cavity, and the density of HSSW responding to both wind-driven latent heat polynya formation and meltwater export from the cavity. Finally, in §5 we summarize our key findings, identify caveats in our approach and avenues for future work, and conclude.

2 A Regional Model of the Southern Weddell Sea and Filchner-Ronne Ice Shelf Cavity

In this section, we provide an overview of the configuration of the Weddell Sea Regional Model (WSRM), describe a reference simulation to illustrate salient aspects of the model, and discuss its evaluation against observational datasets. For a more detailed description of the model setup, including lists of model input parameters, we refer the reader to Hazel (2019). Additional evaluation of the WSRM against observations is provided in the Supporting Information.

2.1 Model Configuration

The WSRM simulates the ocean and sea ice state in the southern Weddell Sea, including the FRIS cavity. The model domain, which is shown in Fig. 1(a), extends from 83.5°S to 64°S latitudinally and from 83.5°W to 21°E longitudinally. Areas west of the Antarctic Peninsula are excluded, as the latitude of the WSRM's northern boundary precludes that part of the ocean from influencing the FRIS in the simulations. The WSRM's northern boundary was placed as far north as possible while excluding the southern flank of the Antarctic Circumpolar Current, which flows approximately parallel to the model domain boundary and would be challenging to represent accurately with open boundary conditions (see below). The WSRM's eastern boundary location was selected to ensure that the model domain includes several hundred kilometers of the continental shelf and slope upstream of the FRIS, allowing the ASF to adjust to surface forcing perturbations (Hattermann, 2018). Antarctic ice sheet topography, ice

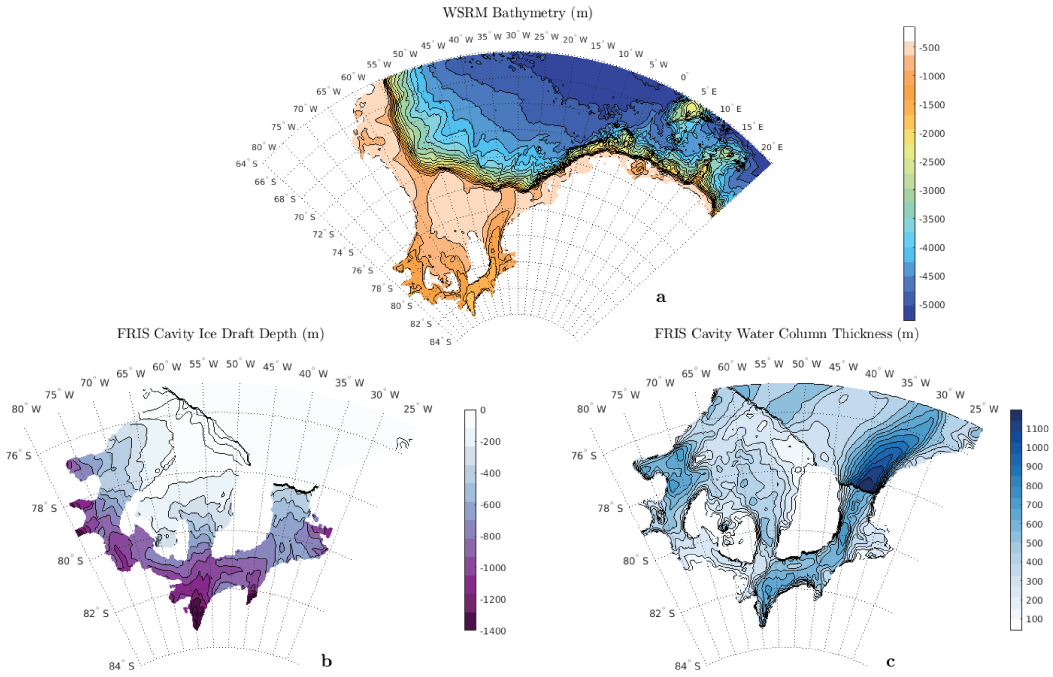

Figure 1: (a) Elevation of the sea floor bathymetry across the entire Weddell Sea Regional Model domain. Enlarged views of (b) the ice shelf draft and (c) water column thickness within the Filchner-Ronne ice shelf cavity.

cavity, and ocean bathymetry in the WSRM are derived from the RTOPO-1 dataset (Timmermann, 2010). For reference, in Fig. 1 we provide a visualization of the bathymetry throughout the WSRM domain, the FRIS ice shelf draft, and the FRIS water column thickness.

The WSRM simulates the evolution of the ocean and sea ice using the Massachusetts Institute of Technology general circulation model (MITgcm) (Marshall, Hill, et al., 1997; Marshall, Adcroft, et al., 1997), checkpoint 65u. The ocean evolves according to the hydrostatic, Boussinesq primitive equations for conservation of momentum, volume potential temperature and salinity, plus an approximation to the full equation of state (Jackett & Mcdougall, 1995). We apply free-slip lateral boundary conditions, and impose a vertical stress at the sea floor and ice shelf base that depends quadratically on the horizontal velocity with coefficient $C_d = 2.1 \times 10^{-3}$. Grid-scale energy and enstrophy are controlled using a dimensionless biharmonic viscosity with coefficient 0.1. Vertical diffusion and mixing are computed via the K-Profile-Parameterization (KPP) scheme (Large et al., 1994). The sea ice evolves according to conservation of momentum, concentration and thickness, with internal stresses parameterized via a viscous-plastic rheology (Hibler III, 1979; Zhang & Hibler III, 1997). The sea ice exchanges momentum with the ocean via a stress that depends quadratically on the ice-ocean shear with coefficient $C_{io} = 5.54 \times 10^{-3}$ (Cole et al., 2014; Park & Stewart, 2016). Thermodynamic exchanges between the sea ice and ocean are modeled via 3-equation thermodynamics (Schmidt et al., 2004). The remaining sea ice model configuration parameters are set to their default values unless stated otherwise (Losch et al., 2010). Ocean-ice shelf exchanges of heat and freshwater are modeled via 3-equation thermodynamics (Losch, 2008), with constant turbulent transfer velocities for heat and salt of $5 \times 10^{-4}\,\mathrm{m/s}$ and $2.5 \times 10^{-6}\,\mathrm{m/s}$, respectively.

The model equations are solved in vector-invariant form and are discretized on a curvilinear latitude/longitude grid. The longitudinal grid spacing is $\frac{1}{3}^{\circ}$, and the latitudinal grid fol-

lows a cosine scaling such that the grid spacing is locally isotropic everywhere in the WSRM domain. This grid allows for finer resolution on the continental shelf and within the ice shelf cavities, where the Rossby radius of deformation and scales of motion are anticipated to be smallest. This grid allows us to run the WSRM across a wide range of forcing parameters (see §4), but carries the caveat that it is too coarse to fully resolve the mesoscale on the continental shelf (St-Laurent et al., 2013; A. L. Stewart & Thompson, 2015a). The ocean is discretized vertically into 139 levels with thicknesses of ∼1 m at the surface to resolve the surface boundary layer (Rocha et al., 2016; A. L. Stewart et al., 2018), and ∼20 m within the FRIS cavity to partially resolve the vertical structure of the ice-ocean boundary layer (de Rydt et al., 2014). At depths of 2000-3000 m the vertical grid spacing reaches ∼50 m over the continental slope and ∼200 m in the deepest portions of the WSRM domain (around 5000 m depth). This grid resolves the first six baroclinic modes in the Weddell Sea (Kial Stewart, *pers. comm.*), based on the number of vertical grid points spaced between the nodes of each baroclinic mode (K. Stewart et al., 2017). Advection of ocean and sea ice tracers is performed using a 7^{th}-order one-step method advection scheme. The model time step is 480 seconds.

The WSRM is forced by a prescribed, evolving atmospheric state over the entire model domain, in addition to a prescribed oceanic state at its open eastern and northern boundaries. The atmospheric state is derived from Antarctic Mesoscale Prediction System (AMPS) (Powers et al., 2012), which is a numerical weather prediction system based on the Polar Weather Research and Forecasting (WRF) model. We use AMPS data from 2007 to 2015 (a total of 9 years), which is provided at horizontal grid spacings of 20 km (Jan 2007–Oct 2008), 15 km (Nov 2008–Dec 2012) and 10 km (Jan 2013–Dec 2015), and is interpolated linearly onto the WSRM's 1/3° grid. Specifically, we prescribe the daily-averaged 10-m zonal and meridional winds, 2-m atmospheric temperature, sea level pressure, longwave and shortwave radiation, precipitation, and relative humidity. MITgcm uses bulk formulae to calculate air-ice and air-ocean fluxes of heat, freshwater, and momentum at every timestep. We use default parameters for these bulk formulae unless otherwise stated (Adcroft et al., 2018). The WSRM's open boundaries are prescribed to follow a repeating, year-long monthly climatology derived from the Southern Ocean State Estimate (SOSE) (Mazloff et al., 2010). The climatology comprises the potential temperature, salinity and horizontal velocity of the ocean, and the thickness, concentration and horizontal velocity of the sea ice. We impose the open boundary conditions via a sponge layer that extends approximately 200km into the model interior, over which the model state is restored toward the boundary fields with inner and outer relaxation timescales of 10 days and 0.5 days, respectively. Additionally, tidal fluctuations of the horizontal velocity fields are imposed at the northern and eastern boundaries. Specifically, we prescribe ten tidal components (M_2, S_2, N_2, K_2, K_1, O_1, P_1, Q_1, M_f, and M_m) using phases and amplitudes derived from the Circum-Antarctic Tidal Solution (CATS) 2008b (Padman et al., 2002).

We initialize the ocean and sea ice states in our simulations using annual-mean properties derived from the Southern Ocean State Estimate (SOSE). SOSE does not include a representation of Antarctic ice shelf cavities, so in these regions we linearly extrapolate from SOSE output data in the open ocean, and then apply a restoring of the potential temperature and salinity over the first two years of each simulation. The restoring step was found to be necessary because the simulation results are sensitive to the initial conditions within the FRIS cavity, as discussed in §3, and because simply initializing the cavity with uniform potential temperature and salinity led to very large velocities and numerical instability. In our reference simulation, we restored the cavity potential temperature to the surface freezing temperature and the cavity salinity to 34.45 psu, with a relaxation timescale of 30 days. We integrate the WSRM until each simulation reaches a statistically steady state, as judged by time series of mean FRIS cavity temperature and salinity. The integrations typically required 20–30 years to reach a statistically steady state, so we cycled the 9-year atmospheric forcing dataset as required.

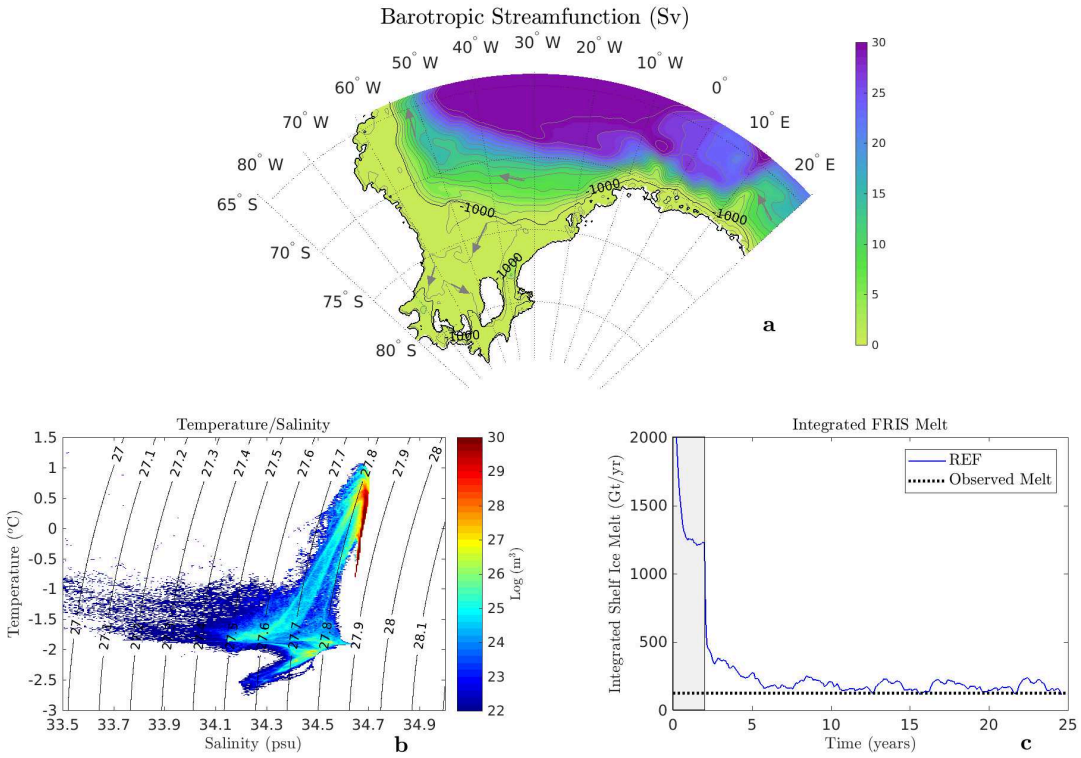

Figure 2: Circulation, hydrography and melt rates in our Weddell Sea Regional Model (WSRM) reference simulation. (a) Barotropic streamfunction with streamlines overlaid as gray contours (.5 Sv contour interval) and bathymetric contours overlaid as black contours (1000 m contour interval). (b) Temperature/salinity diagram of the physical volume occupied by each potential temperature/salinity bin throughout the full model domain. A bin size of 0.07 psu by 0.05°C was used. Contours indicate surface-referenced potential density (.1 kg/m^3 contour interval). (c) Time series of area-integrated Filchner-Ronne Ice Shelf (FRIS) melt rate. The dotted black line represents the observed FRIS melt rate of 124 Gt/yr (Moholdt et al., 2014). The shaded gray region in panel (c) indicates the 2-year period over which the FRIS cavity is restored to a salinity of 34.45 psu and to the surface freezing temperature. The data in panels (a) and (b) is drawn from an average over the last 9-year WSRM forcing cycle in the reference simulation (years 10–18).

2.2 Simulated Circulation and Model Evaluation

We now discuss the simulated ocean state and circulation in our WSRM reference simulation to provide context for the results of the perturbation simulations discussed in §3 and §4. All diagnostics discussed here were averaged over the last full 9-year atmospheric forcing cycle in the reference simulation (years 10–18). Fig. 2(a) illustrates the simulated circulation via the barotropic streamfunction throughout the WSRM domain. A relatively strong (∼20 Sv) Antarctic Slope Current visibly follows the isobaths of the continental slope westward from the eastern boundary, around the southern and western edges of the Weddell Gyre, and then northward through the northern boundary. This circulation is largely inherited from SOSE via the WSRM open boundary conditions. In the FRIS cavity a weak (∼0.5 Sv) anticyclonic circulation is visible, with fluid entering the cavity at the western edge of the ice shelf face (around 75°S, 60°W) and leaving through the Filchner trough (around 78°S, 40°W). This circulation is qualitatively consistent with previous estimates (Gerdes et al., 1999; Jenkins & Holland, 2002; Nicholls et al., 2009). The cavity circulation will be examined more closely in §3.

In Fig. 2(b) we visualize the simulated water masses via a temperature/salinity (T/S) plot, with colors indicating the physical volume of the model domain occupied by each T/S bin. The distribution of water masses conforms to observations made in the southern Weddell Sea, although HSSW is biased fresh by around 0.2 psu compared to observations (Nicholls et al., 2009). This fresh HSSW anomaly in the WSRM may be an artifact of the model resolution; as a finer horizontal grid would allow ice to respond to more localized atmospheric and oceanic forcing and resolve smaller-scale polynyas and cracks in the ice (Newsom et al., 2016). Another possibility for the fresh HSSW anomaly is that meridional winds derived from AMPS may be under-resolved, especially in regions along the coast with steep orography (Bintanja et al., 2014). We explore the latter point further in §4. Fig. 2(b) also exhibits waters below the surface freezing temperature, which result from HSSW circulating through the FRIS cavity and melting the ice shelf (Darelius & Sallee, 2018). This "mode 1" melting (Dinniman et al., 2016) is anticipated to produce relatively low rates of ice shelf mass loss, as HSSW is typically only a few tenths of one °C above the local freezing temperature at the FRIS base. In Fig. 2(c) we plot a time series of the area-integrated FRIS melt over the entire duration of our reference simulation. For the first two years, as the FRIS cavity is restored to the surface freezing temperature everywhere, the FRIS cavity approaches a relatively high melt rate of $\sim$1200 Gt/yr. After the two-year restoring period, HSSW is able to enter the cavity and model adjusts to a more modest melt rate of $\sim$200 Gt/yr, as shown in Fig. 2(c); this melt rate is slightly outside the observational uncertainty of 58–190 Gt/yr (Moholdt et al., 2014).

We have performed additional evaluation of the WSRM reference simulation against observational datasets, as described in the Supporting Information (SI). Specifically, we compare the simulated hydrography against measurements from the WOCE A12 and SR4 sections and to a hydrographic climatology derived from ship and tagged seal data in the vicinity of 17°W (Hattermann & Rohardt, 2018), we compare the simulated sea surface elevation against measurements derived from CryoSat-2 (Armitage et al., 2018), and we compare the simulated sea ice concentration against satellite-derived measurements (Lavergne et al., 2019). In general, the ocean/sea ice state simulated by the WSRM is qualitatively and quantitatively similar to the observations. Salient differences include a shallowing of the ASF in the reference simulation relative to the observed hydrography, and differences in the simulated sea ice concentration in the vicinity of the model's open boundary conditions. Additionally, the austral Spring sea ice concentration is higher by up to 30% in the vicinity of the Ronne ice shelf, suggesting an under-representation of the Ronne polynya that likely explains the fresh bias in HSSW. We conclude that the WSRM reproduces the key features of the southern Weddell Sea and FRIS cavity circulation, with further improvements likely if the model were run with a finer horizontal grid.

3 Bi-Stability of the FRIS Cavity Circulation

In this section, we investigate the dependence of the FRIS cavity circulation, melt rate, and water mass properties on initial FRIS cavity conditions. As described in §2, for the first two years of a simulation, FRIS cavity properties are restored on a 30-day timescale to the surface freezing temperature and to a specified salinity, S_r. We first show in §3.1 that the equilibrated state of the WSRM is strongly sensitive to S_r, suggesting that the model supports two stable equilibria for the same atmospheric and boundary conditions. In §3.2 we perform experiments with modified atmospheric forcing to investigate the sensitivity of these states to external forcing perturbations.

3.1 Dependence of FRIS Melt Rates on Pre-Existing Cavity Conditions

We now compare a pair of WSRM experiments that differ only in their initial conditions, as defined by the relaxation salinity in the cavity, S_r: in our reference experiment "REF" we use $S_r = 34.45$ psu, and in our perturbation experiment "FRESH" we use $S_r = 34$ psu. In both experiments the cavity restoring is applied only over the first 2 years of model integration, and

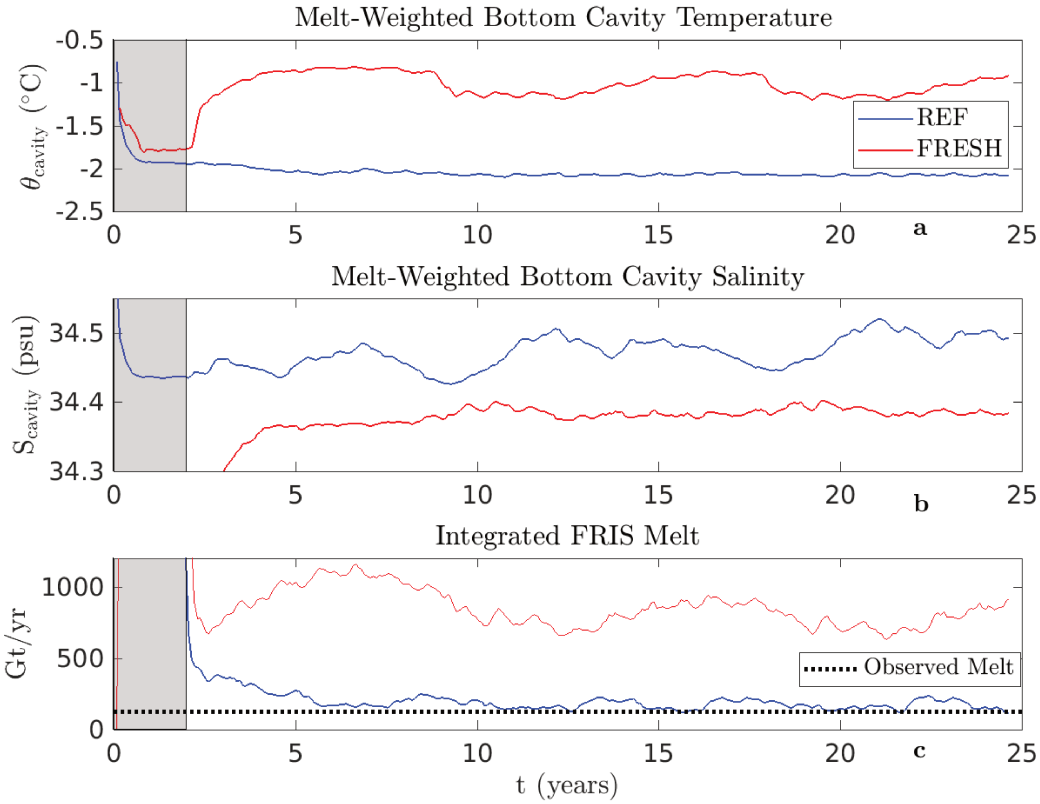

Figure 3: Time series of Filchner-Ronne cavity properties and ice shelf melt rates in our reference simulation (REF, blue curves) and a simulation with fresher initial conditions within the cavity (FRESH, red curves). (a) Melt-weighted bottom cavity potential temperature θ_{cavity} (°C), (b) melt-weighted bottom cavity salinity S_{cavity} (psu), and (c) area-integrated FRIS melt (Gt/yr). The reader is referred to §3.1 for definitions. The shaded region corresponds to the two-year FRIS cavity restoring period at the start of each simulation. The dotted black line in (c) corresponds to the observed melt rate from Moholdt et al. (2014).

then integration is continued until the model reaches a statistically steady state over a full 9-year atmospheric forcing cycle. In Fig. 3(c) we plot time series of the area-integrated FRIS basal melt rates over the course of the REF and FRESH experiments. Whereas the basal melt rate in REF falls to ∼200 Gt/yr after 25 years, in FRESH it remains much higher at ∼800 Gt/yr.

To explain the difference between REF and FRESH, in Fig. 4 we compare the barotropic streamfunctions, sea floor potential temperatures and basal melt rates between these experiments. Fig. 4(a–b) shows that the circulation within the cavity is substantially stronger in FRESH, with a cavity-spanning transport of around 2 Sv and a local re-circulation of around 5 Sv in the Filchner trough. Moreover, the direction of the circulation in FRESH is opposite to that in REF: in FRESH, waters enter the cavity at the eastern edge of the ice shelf face, and exit at the western side. The sea floor potential temperature distributions in Fig. 4(c–d) reinforce this conclusion: in REF, the warmest waters are found close to the western side of the ice shelf face, whereas in FRESH they are found closer to the eastern side. This suggests that the inflow of HSSW from the western edge of the FRIS face has been displaced by an inflow of mWDW from the eastern edge of the FRIS face. Fig. 4(e–f) shows that highest melt rates are generally found in similar locations in both experiments; these locations largely correspond to the

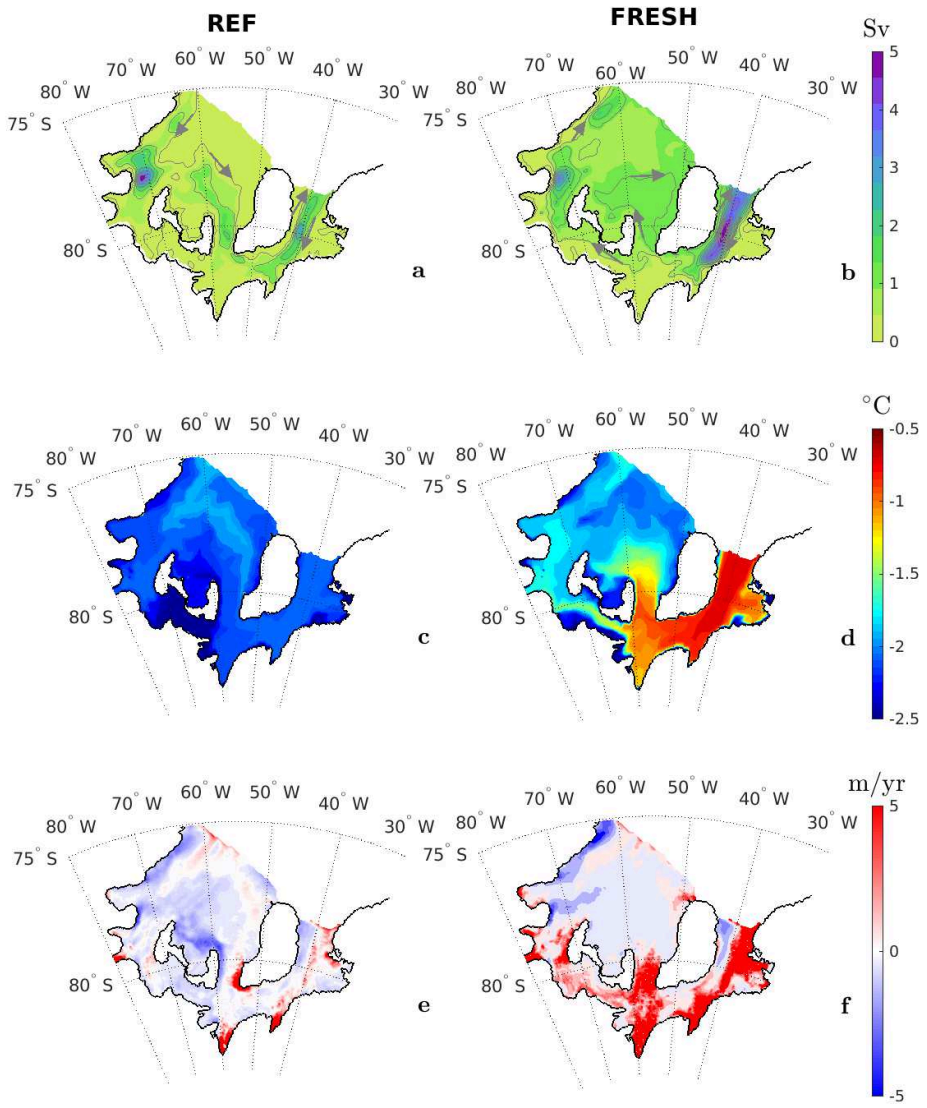

Figure 4: Comparison of the simulated Filchner-Ronne Ice Shelf (FRIS) cavity state in our (a,c,e) REF and (b,d,f) FRESH simulations. (a,b) Barotropic streamfunction (Sv). Gray contours correspond to streamlines with a spacing of .5 Sv. (c,d) Sea floor potential temperature (°C). (e,f) Ice shelf melt rates (m/yr). All plotted quantities have been averaged over model years 10–18.

deepest parts of the ice shelf draft (see Fig. 1) and so experience the strongest thermal forcing from warm, dense waters that intrude into the cavity. An exception is that the melt rates in FRESH are substantially higher in the central and eastern Filchner Trough.

We now relate the difference in melt rates between REF and FRESH to differences between the simulated cavity temperatures, for which we require a metric for cavity-averaged properties such as potential temperature and salinity. Much of the cavity volume is filled with waters very close to the sea floor temperature, so metrics such as the volume-averaged potential temperature and salinity do not clearly distinguish between the cavity properties in the REF and FRESH cases. Based on the expectation that the waters circulating through the FRIS cav-

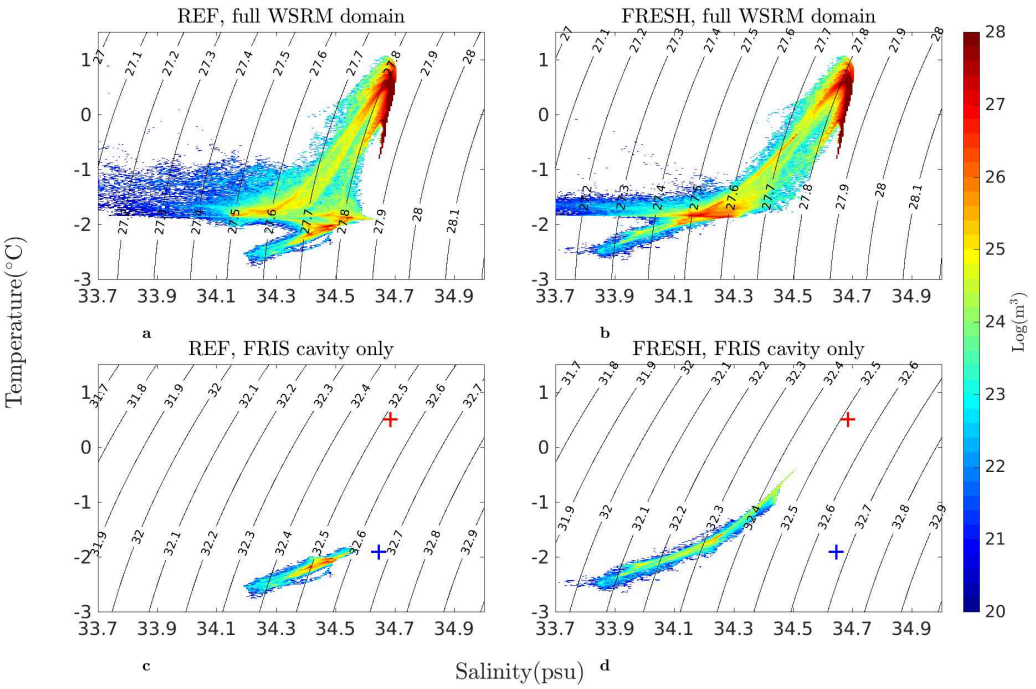

Figure 5: Temperature/salinity diagrams for our (a,c) REF and (b,d) FRESH experiments. Colors indicate the physical volume occupied by each potential temperature/salinity bin throughout the (a,b) the full model domain and (c,d) the Filchner-Ronne Ice Shelf cavity only. A bin size of 0.07 psu by 0.05°C was used in all plots. Contours indicate potential density (.1 kg/m^3 contour interval) referenced (a,b) to the surface and (c,d) to 1000 dbar. All data were drawn from an average over model years 10–18 Red and blue crosses in (c,d) indicate the core of the Warm Deep Water offshore and the densest High Salinity Shelf Water on the continental shelf (in REF), respectively. Values represent averages over years 10–18.

ity and melting the ice shelf are denser than the resulting meltwater, we therefore define our metric based on an average over the sea floor within the FRIS cavity. However, even when the total FRIS melt rate is elevated, the melt rates are still largely localized to a few, deep areas of the cavity (see Fig. 4(e–f)), so an average over the entire cavity floor does not capture the properties of the intruding water masses. We therefore weight our average over the sea floor by the local melt rates at each horizontal location. More precisely, for an arbitrary property ϕ we define its "melt-weighted" average as

$$\phi_{\text{cavity}} \equiv \frac{\int_{\overline{F_{\text{melt}}}^t > 0} \overline{\phi_{\text{bot}}}^t \, \overline{F_{\text{melt}}}^t \, \mathrm{d}A}{\int_{\overline{F_{\text{melt}}}^t > 0} \overline{F_{\text{melt}}}^t \, \mathrm{d}A}. \tag{1}$$

Here the overline $\overline{\bullet}^t$ denotes a time average, which is taken over one month unless otherwise stated, ϕ_{bot} denotes the value of property ϕ at the sea floor, F_{melt} denotes the downward freshwater flux, and dA denotes an infinitesimal horizontal area.

In Fig. 3, we plot time series of the melt-weighted cavity bottom potential temperature θ_{cavity} and salinity S_{cavity}. This shows that the greatly increased melt rate in FRESH corresponds to a much warmer cavity temperature; in FRESH θ_{cavity} equilibrates to around 1°C above the surface freezing temperature, whereas in REF θ_{cavity} is around $-2.1\,^\circ$C. There is also a substantial difference in the cavity salinities between the experiments, with REF equilibrating around

0.1 psu higher than FRESH (∼34.5 psu vs. ∼34.4 psu). Taken together these diagnostics indicate that our imposed freshening of the waters in the cavity at the start of the simulation leads to waters of substantially lower density than HSSW flooding the cavity in equilibrium. This suggests that dense HSSW is absent in FRESH, but continues to form unabated in REF.

To determine how the FRIS cavity water masses have changed between the REF and FRESH experiments, in Fig. 5 we compare T/S diagrams for REF and FRESH side-by-side. The most striking difference between the water mass properties is that there is no longer any distinguishable HSSW in the FRESH experiment (Fig. 5(a–b)). This results in an overall freshening and warming of the waters in the FRIS cavity ((Fig. 5(c–d)). In Fig. 5(c–d) we additionally plot the T/S properties of the saltiest HSSW in REF (blue marker) and of the core of the offshore WDW (red marker). The T/S structure in Fig. 5(c) indicates that the cavity waters result from melting of the underside of the ice shelf by HSSW (Gade, 1979; Darelius & Sallee, 2018). In contrast, Fig. 5(d) indicates that the waters entering the FRIS cavity are ultimately sourced from the WDW offshore, but have been transformed into mWDW as by the time they reach the southern Weddell Sea continental shelf.

Taken together, these diagnostics suggest that imposing a fresher initial FRIS cavity state in FRESH leads to intrusions of mWDW that result in an absence of dense HSSW, due to entrainment of ice shelf meltwater. In contrast, the saltier initial cavity state in REF allows HSSW to form and flood the cavity, preventing mWDW from intruding beneath the FRIS. This results in FRESH equilibrating to a state with relatively high basal melt rates, and REF equilibrating to a state with relatively low basal melt rates. All of our other perturbation experiments (see §3.2 and §4) equilibrate to one of these two states, which we henceforth refer to as the "warm state" and "cold state" of the FRIS cavity, respectively.

3.2 Sensitivity to Surface Forcing Perturbations

In §3.1 we established that pre-existing conditions in the FRIS cavity strongly influence the steady-state circulation, melt rate, and water mass properties within the cavity. Next, we explore the potential for changes in the local atmospheric state to induce transitions between the "cold" and "warm" FRIS states. Specifically, we investigate whether idealized perturbations to the atmospheric forcing in the REF experiment can push the model from a low-melt state to something closer to the high-melt state simulated in the FRESH experiment, and vice versa. We conduct series of atmospheric forcing perturbation experiments via idealized modifications of the 2-meter temperature, the 10-meter meridional wind, and the 10-meter zonal wind. We expect changes in the atmospheric temperature and the meridional winds to modify the rate of sea ice and HSSW formation (Nicholls et al., 2009); cooling the atmosphere and/or increasing the northward wind speed may be expected to produce denser HSSW and transition the cavity from a warm to a cold state, and *vice versa*. We also expect increases in the westward to wind stress to increase the strength of the ASF by increasing the rate of Ekman overturning (Nøst et al., 2011; A. L. Stewart & Thompson, 2015a). Given the role of the ASF as a barrier between shelf waters and warmer WDW (Jacobs, 1991), increasing the westward wind stress may be expected to suppress access of WDW to the FRIS cavity and thus transition the cavity from a warm to a cold state, and *vice versa* (Hattermann, 2018).

We list our atmospheric perturbation experiments in Table 1. This represents a subset of a larger suite of experiments, from which we have selected the extreme perturbations in the interest of a concise presentation. In the wind perturbation experiments, we change the meridional or zonal component of the 10-meter wind speed by a constant factor, and in the atmospheric temperature perturbation experiment, we apply a constant offset to the 2-meter atmospheric temperature. These perturbations are applied everywhere in the model domain, and throughout the 9-year atmospheric forcing cycle. All perturbation experiments were initialized from the end of year 18 in the REF or FRESH simulations, and are integrated until they have again reached a statistically steady state. Time series of the area-integrated FRIS basal melt rates for these experiments are shown in Fig. 6.

Table 1: Experimental Atmospheric Forcing Perturbations

Initial FRIS Cavity State	Atmospheric State Perturbation
Cold (REF)	Zonal Winds 0 %
Cold (REF)	Meridional Winds -50%
Warm (FRESH)	Atmospheric Temperature -30°C
Warm (FRESH)	Meridional Winds +20%

First, we discuss two experiments initialized from REF, *i.e.* starting from a cold FRIS state. In the first experiment the zonal winds are set to zero, while in the second experiment the meridional winds are reduced by 50%. Following the discussion above, we expected both of these perturbations to favor increased mWDW access to the FRIS cavity: weakening the easterly winds would reduce the strength of the ASF and increase the corresponding heat transfer towards the ice shelves. Contrary to these expectations, removing the zonal winds did not substantially impact the FRIS cavity melt rate, which remains relatively low ($\sim$200 Gt/yr) after 20 years of simulation time. In contrast a 50% reduction in the meridional wind strength was sufficient to shift FRIS cavity from the cold state to the warm state (melt rates approaching 1000 Gt/yr) within $\sim$15 years (see Fig. 6).

Next, we discuss two experiments initialized from FRESH, *i.e.* starting from a warm FRIS state. In the first experiment we decrease the atmospheric temperature by -30°C, while in the second experiment, we increase the strength of the meridional winds by 20%. Both of these perturbations are anticipated to increase HSSW production and prevent mWDW from accessing the FRIS cavity. Whereas one might expect a 30°C decrease in atmospheric temperature to increase ocean surface heat loss, we instead found that it did not substantially alter the melt rate, which remains steady around 700 Gt/yr. In contrast, increasing the strength of the meridional winds by just 20% is sufficient to shift the FRIS cavity from its initial warm state to a cold state over 25 years.

Taken together, these perturbation experiments indicate that changes in the meridional wind strength are particularly effective in switching the FRIS cavity between warm and cold states. This is likely due to changes in the rate of wind-driven ice movement away from the front of the FRIS, and associated changes in the formation of HSSW. In §4 we therefore perform a more focused set of perturbation experiments to test this hypothesis.

4 Offshore Wind-Mediated Transitions in FRIS Cavity Melt Rates

Motivated by the results presented in §3, we now perform a series of meridional wind perturbation experiments to identify transitions between the "warm" and "cold" FRIS states. These transitions define the range of meridional wind strengths over which the FRIS is bi-stable, *i.e.* for which either the warm or the cold FRIS cavity states can occur depending on the initial conditions in the cavity. We then pose a conceptual model to explain this behavior, in which the denser of HSSW or mWDW invades the FRIS cavity. A positive feedback between the temperature of the invading water mass and the rate of freshwater export from the FRIS gives rise to bi-stability over a range of wind stress perturbations, forming a hysteresis loop.

4.1 Meridional Wind Perturbation Experiments

The formulation of our meridional wind perturbation experiments follows that described in §3.2. We define a parameter χ that quantifies the amplitude of the winds relative to those

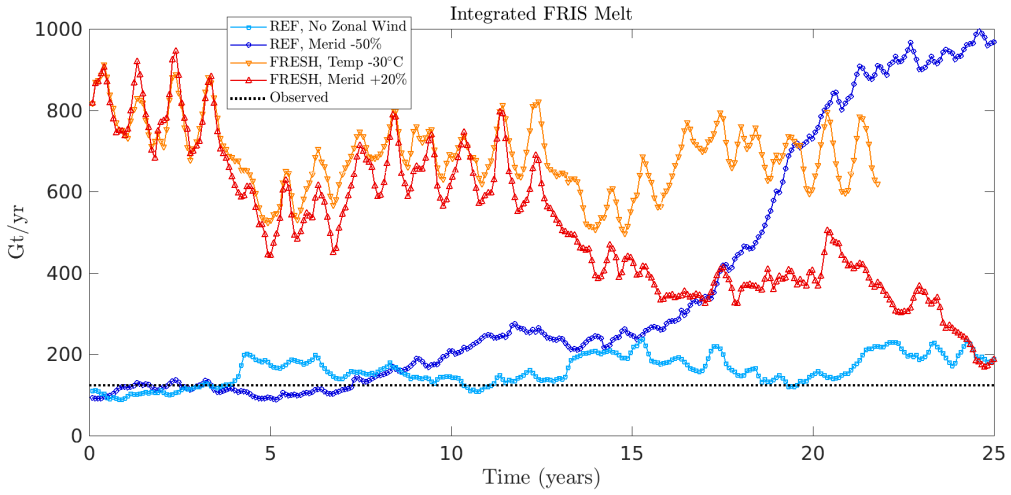

Figure 6: Time series of area-integrated Filchner-Ronne Ice Shelf melt rates (Gt/yr) in our atmospheric perturbation experiments. The dotted black line indicates the observed FRIS melt rate from Moholdt et al. (2014).

used in our reference simulations. More precisely, we impose

$$V_{\text{wind}} = \chi V^0_{\text{wind}}, \tag{2}$$

where V_{wind} and V^0_{wind} are the meridional components of the 10-meter winds in the perturbation experiment and the reference experiment, respectively. Based on the results in §3.2, we examine values of χ ranging from .5 (-50% wind strength) to 1.2 (+20% wind strength). For each value of χ, we initialize one experiment from the end of year 18 in REF, *i.e.* starting from a cold state ("cold-start" experiments), and one experiment from the end of year 18 in FRESH, *i.e.* starting from a warm state ("warm-start" experiments). Each simulation is run until a new statistically steady state, as judged by time series of the area-integrated FRIS melt rate, θ_{cavity}, and S_{cavity}, is reached for a minimum of nine years, which corresponds to the length of the WSRM atmospheric forcing repeat cycle.

In Fig. 7 we plot the area-integrated FRIS basal melt rates and the melt-weighted cavity bottom potential temperature (θ_{cavity}) and salinity (S_{cavity}) as functions of χ. All time averages, including those in equation (1), are taken over the last complete 9-year atmospheric forcing cycle in each experiment. As expected from our atmospheric perturbation experiments in §3.2, both the cold-start and warm-start experiments equilibrate to a cold cavity state (melt rates of $\sim$200 Gt/yr) for sufficiently strong meridional winds ($\chi \geq 1.15$), and equilibrate to a warm cavity state (melt rates of $\sim$1000 Gt/yr and $\theta_{\text{cavity}} \gtrsim -1°$C) for sufficiently weak meridional winds ($\chi \leq 0.6$). For intermediate wind perturbations ($0.7 \leq \chi \leq 1.1$) the FRIS cavity is bi-stable, *i.e.* the simulations can equilibrate to either a warm state (melt rates of 600–800 Gt/yr and $\theta_{\text{cavity}} \approx -1°$C) or a cold state (melt rates of $\sim$150Gt/yr and $\theta_{\text{cavity}} \approx -2°$C), depending on the initial conditions. Thus the FRIS cavity exhibits a hysteresis: for example, if the FRIS cavity were initialized in a cold state and the winds were gradually reduced in amplitude from $\chi = 1$ to $\chi = 0.5$, Fig. 7 suggests that the cavity would abruptly switch over to a warm state somewhere between $\chi = 0.6$ and $\chi = 0.7$. However, in order to return to the cold state the wind strength would then need to be increased much more, to $\chi \gtrsim 1.15$. This mirrors the results of Hellmer et al. (2017), who found that switching back to a 20$^{\text{th}}$-century climate after imposing 21$^{\text{st}}$-century atmospheric conditions did not revert the FRIS to 20$^{\text{th}}$-century melt rates.

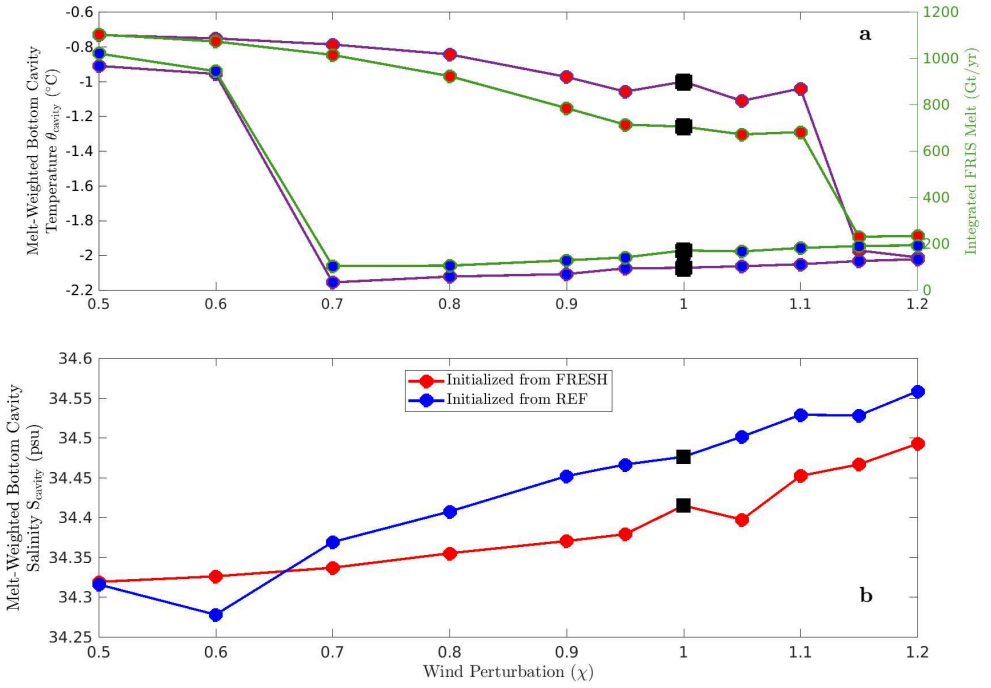

Figure 7: (a) Area-integrated Filchner-Ronne Ice Shelf (FRIS) melt rates (green lines) and melt-weighted cavity bottom temperature, θ_{cavity} (purple lines), and (b) melt-weighted cavity bottom salinity, S_{cavity}, as functions of the dimensionless meridional wind perturbation, χ. All quantities are averaged over the last full 9-year atmospheric forcing cycle in each simulation. Black squares indicate the REF and FRESH experiments, discussed in §3. Red and blue dots indicate simulations initialized with the FRIS cavity in a warm and cold states (from the FRESH and REF simulations), respectively.

In §3, we inferred that the shift between cold and warm states occurred due to the water mass flooding the FRIS cavity shifting between HSSW and mWDW. In Fig. 8 we examine changes in the cavity water masses via T/S plots for a subset of our meridional wind perturbation experiments. Together with Fig. 7, this suggests that in all simulations with warm FRIS states, the waters within the cavity are sourced from mWDW, and that in all simulations with cold FRIS states, the waters within the cavity are sourced from HSSW. Varying the wind perturbation χ leads to modest changes in the T/S properties of the cavity water masses in both Fig. 8 and Fig. 7: within the cold-state experiments, θ_{cavity} varies by around 0.1°C and the FRIS melt rate varies by approximately a factor of 2, while within the warm-state experiments θ_{cavity} varies by around 0.25°C and again the FRIS melt rate varies by approximately a factor of 2. However, the changes in cavity salinity between experiments correspond to much larger density variations than do the changes in cavity temperature: S_{cavity} varies by around 0.13 psu between experiments that simulate a warm FRIS cavity state, and by around 0.18 psu between experiments that simulate a cold FRIS cavity state. The latter is consistent with HSSW of increasingly high salinity flooding the cavity with increasing offshore wind strength, sea ice production and brine rejection along the front of the FRIS.

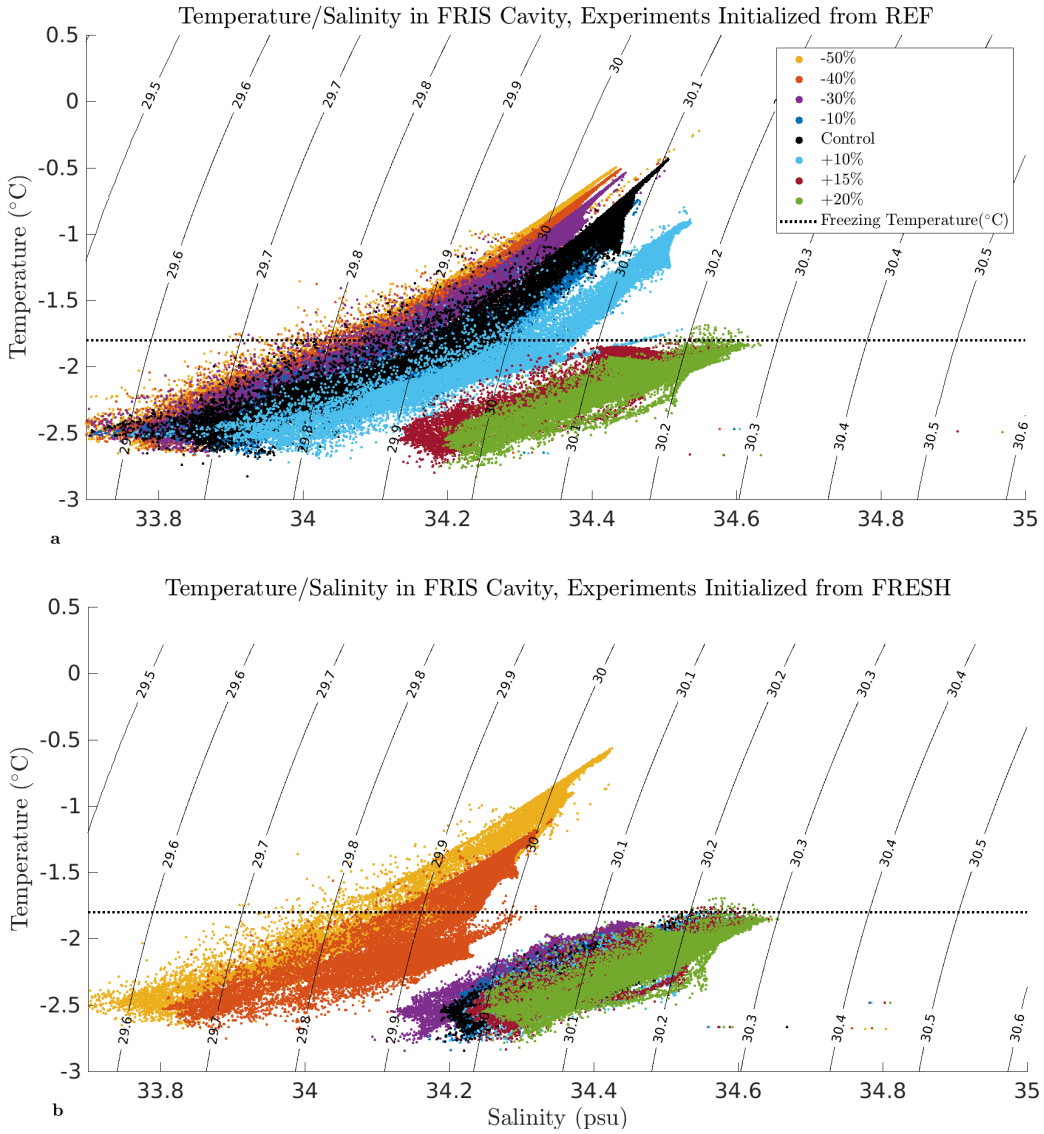

Figure 8: Overlapping temperature/salinity diagrams showing properties of waters within the Filchner-Ronne Ice Shelf (FRIS) cavity in a subset of our meridional wind perturbation experiments (see §4). (a) Experiments initialized from the REF experiment, *i.e.* with a "cold" initial FRIS state. (b) Experiments initialized from the FRESH experiment, *i.e.* with a "warm" initial FRIS state. The plotted points correspond to a sub-sample of the full FRIS cavity, derived by sampling every 10^{th} model gridpoint after averaging over the last 9-year atmospheric forcing cycle. Black contours correspond to potential density referenced to 500 dbar to facilitate comparison of water mass densities at the approximate depth of the FRIS cavity mouth. The dotted horizontal black line indicates the surface freezing temperature.

4.2 A Conceptual Model of FRIS Bi-Stability

Our offshore wind perturbation experiments in §4 demonstrate that there is a range of meridional wind strengths over which the FRIS is bi-stable, *i.e.* for which both cold and warm FRIS cavity states can occur, depending on the initial conditions. Furthermore, our analysis of integrated melt rate and melt-weighted bottom salinity and temperature in Fig. 7 suggests

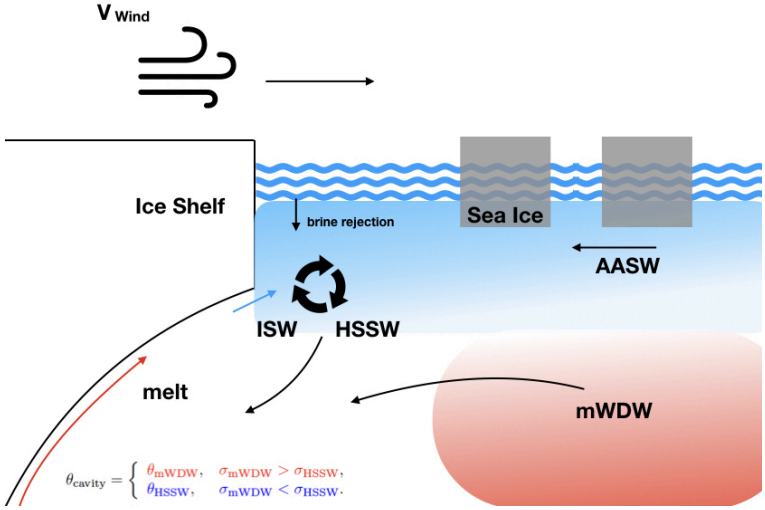

Figure 9: A schematic of the ice-shelf ocean interface that highlights the key water masses and mechanisms involved in our conceptual model. Offshore, the upper water column is occupied by Antarctic Surface Waters (AASW), which we use for simplicity to refer to any waters lighter than WDW. At greater depths, the water column is occupied by warmer and saltier Warm Deep Water (WDW), which is modified as it intrudes onto the continental shelf to become modified WDW (mWDW). At the coastline, offshore winds blow sea ice offshore, inducing latent heat polynya formation, brine rejection, and High Salinity Shelf Water (HSSW) formation. We postulate that either HSSW or mWDW floods the ice shelf cavity, depending on which is denser. The resulting melting of the ice shelf base forms ISW, which mixes with HSSW and modifies its salinity.

that the warm and cold states manifest due to the cavity being flooded by either mWDW or HSSW, respectively. We now pose a conceptual model to explain the FRIS bi-stability, in which the denser of HSSW or mWDW floods the cavity, and the feedback between the cavity melt rate and the salinity of HSSW gives rise to two distinct stable states.

The key elements of our conceptual model are illustrated in Fig. 9. Offshore of the FRIS, the salient components of the ocean stratification are a relatively cold, fresh layer of Antarctic Surface Waters (AASW), which we use to refer to any waters lighter than WDW, including Winter Waters (WW). This overlies a warmer, saltier WDW layer, which arrives on the continental shelf as mWDW. On the continental shelf, offshore winds advect ice away from the coast and create latent heat polynyas (Smith et al., 1990; Tamura et al., 2016), releasing brine and transforming AASW into HSSW (Nicholls et al., 2009). A defining aspect of our model is that either HSSW or mWDW floods the FRIS cavity, depending on which of the two is denser. More precisely, the potential temperature of the densest waters in the cavity is determined as follows,

$$\theta_{\text{cavity}} = \begin{cases} \theta_{\text{mWDW}}, & \sigma_{\text{mWDW}} > \sigma_{\text{HSSW}}, \\ \theta_{\text{HSSW}}, & \sigma_{\text{mWDW}} < \sigma_{\text{HSSW}}. \end{cases} \tag{3}$$

Here σ is the locally-referenced potential density at the cavity mouth, which will be defined specifically later in this section. Thus, if $\sigma_{\text{HSSW}} < \sigma_{\text{mWDW}}$ then relatively warm mWDW floods the FRIS cavity, corresponding to the warm state defined by the upper "branch" of the hysteresis loop in Fig. 7. If $\sigma_{\text{HSSW}} > \sigma_{\text{mWDW}}$ then HSSW floods the FRIS cavity, corresponding to the cold state defined by the lower "branch" of the hysteresis loop in Fig. 7.

Evaluating equation (3) requires knowledge of the potential temperatures and salinities of both HSSW and mWDW, respectively, *i.e.* θ_{HSSW}, θ_{mWDW}, S_{HSSW} and S_{mWDW}. Fig. 7 sug-

gests that of these four, S_{HSSW} exhibits the largest dynamical variations, *i.e.* defined by the impact of these variations on water mass density, as discussed in §4.1. In the interest of simplicity we therefore assume that θ_{mWDW}, S_{mWDW} and θ_{HSSW} are constants, and do not give further consideration to what sets these constants (see Table 2). We also neglect transformation that occurs as HSSW and mWDW make their way into the FRIS cavity, which tend to make these water masses fresher and colder (see Fig. 5). Consequently, the selected values of θ_{mWDW}, S_{mWDW} and θ_{HSSW} are all lower than they would be if they were measured, for example, beneath the Ronne polynya or within the Filchner Trough. We then posit that S_{HSSW} depends upon the ambient salinity of AASW, salt input from brine rejection, and freshwater that emerges from the FRIS cavity,

$$S_{\mathrm{HSSW}} = S_{\mathrm{AASW}} + \Delta S_{\mathrm{polynya}} - \Delta S_{\mathrm{melt}}. \tag{4}$$

In equation (4), S_{AASW} is the salinity of AASW, which is assumed to be constant, $\Delta S_{\mathrm{polynya}}$ quantifies the increase in salinity due to salt input from brine rejection in the ice-front polynya, and ΔS_{melt} quantifies the decrease in salinity due to meltwater export from beneath the FRIS.

We first discuss the formulation of $\Delta S_{\mathrm{polynya}}$. In the Weddell, latent heat polynyas occur primarily adjacent to the Ronne Ice Shelf during wintertime, when offshore winds are strongest (Comiso & Gordon, 1998; Tamura et al., 2016). Our $\Delta S_{\mathrm{polynya}}$ quantifies the effect of the resulting brine rejection on the salinity of HSSW as follows,

$$\Delta S_{\mathrm{polynya}} \equiv \frac{\Sigma_{\mathrm{polynya}}}{\rho_0 \Psi}. \tag{5}$$

Here $\Sigma_{\mathrm{polynya}}$ is the area-integrated downward surface salt flux in front of the Ronne Ice Shelf, Ψ is the rate of water mass transformation from AASW to HSSW in m^3/s, and ρ_0 is a reference density. The rate of water mass transformation is assumed to be constant for simplicity, and is anticipated to be $\sim$1 Sv based on the strength of the barotropic circulation in the cavity (see Fig. 4). For calculations below we use an empirically-selected value of $\Psi = 1.3\,\mathrm{Sv}$.

For each of our meridional wind perturbation experiments, we compute $\Sigma_{\mathrm{polynya}}$ as an integral over an area in front of the Ronne Ice Shelf that approximately follows that defined by Haid and Timmermann (2013) (see Supporting Information). We found that it was necessary to extend this area beyond the Ronne polynya (Tamura et al., 2008), over much of the southwestern Weddell continental shelf, to account for the diagnosed changes in S_{HSSW}. Fig. 10(a) shows that across our experiments, $\Sigma_{\mathrm{polynya}}$ closely adheres to a linear relationship with the meridional wind strength, as quantified by our wind perturbation parameter χ:

$$\Sigma_{\mathrm{polynya}} \equiv \Sigma^0_{\mathrm{polynya}} + C_{\mathrm{polynya}} \cdot \chi. \tag{6}$$

Based on Fig. 10, we select $\Sigma^0_{\mathrm{polynya}} = -2.0 \times 10^8\,\mathrm{g/s}$ and $C_{\mathrm{polynya}} = 5.5 \times 10^8\,\mathrm{g/s}$ as the coefficients of this linear fit. The linear dependence of $\Sigma_{\mathrm{polynya}}$ on wind strength (χ) may be rationalized as follows: the growth rate of ice is a function of the exposure, in time and temperature, of ice to the atmosphere (Petrich & Eicken, 2017). Assuming that sea ice drift varies linearly with wind speed (Thorndike & Colony, 1982), for example as in the case of free drift (Leppäranta, 2011), it follows the rate at which the ocean surface is exposed to the atmosphere, and thus the rate of sea ice formation and brine rejection, should also vary linearly with χ. Note that the non-zero offset in the linear fit, $\Sigma^0_{\mathrm{polynya}}$, suggests that the relationship between $\Sigma_{\mathrm{polynya}}$ and χ would become nonlinear if sufficiently weak meridional winds were imposed.

We now discuss the formulation of ΔS_{melt}. As discussed in §3, the simulated FRIS undergoes melting due to circulation of HSSW or mWDW within the cavity, though locally seawater may either melt or freeze onto the ice shelf base. We assume that the net freshwater input into the ocean mixes with HSSW during its formation process. The freshwater flux due to melt is therefore assumed to decrease the salinity of HSSW according to

$$\Delta S_{\mathrm{melt}} \equiv \frac{f_{\mathrm{melt}} \Sigma_{\mathrm{melt}}}{\rho_0 \Psi}. \tag{7}$$

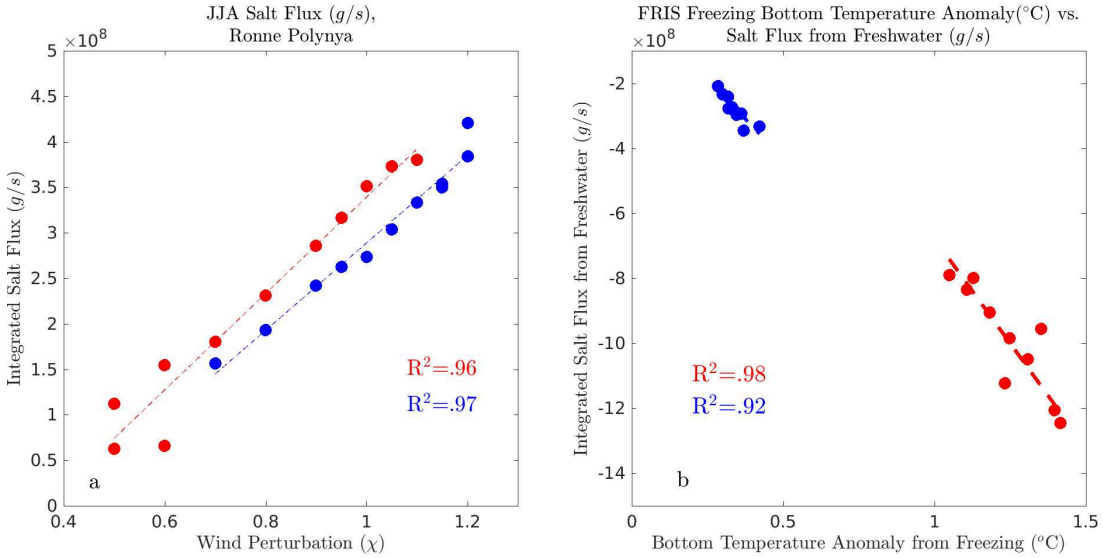

Figure 10: Variation of salt fluxes contributing to High Salinity Shelf Water (HSSW) formation across our suite of meridional wind perturbation experiments. (a) Downward salt flux integrated over the ocean surface and averaged over June-July-August near the Ronne ice shelf (see Supporting Information), plotted against the wind perturbation parameter χ. (b) Equivalent downward salt flux due to area-integrated melting/freezing at the base of the Filchner-Ronne ice shelf, plotted as a function of the melt-weighted cavity temperature anomaly above freezing. All averages were taken over the last 9-year atmospheric forcing cycle in each model simulation. Red dots represent simulations that equilibrate to a warm FRIS cavity steady-state, and blue dots represent simulations that equilibrate to a cold FRIS cavity steady-state (see Fig. 7).

This equation is almost identical to (5), except Σ_{melt} is the equivalent salt loss associated with the FRIS area-integrated time-averaged meltwater input. However, much of the Ice Shelf Water currently formed via basal melt leaves the FRIS cavity as a deep plume (Grosfeld et al., 2001). We assume that only a fixed fraction f_{melt} of the meltwater mixes with and freshens HSSW, where f_{melt} is chosen empirically. As discussed in §2, our formulation of the ocean-to-ice shelf heat flux uses a constant turbulent transfer velocity (Jenkins et al., 2001; Losch, 2008). We might therefore anticipate an approximately linear relationship between Σ_{melt} and the cavity temperature θ_{cavity},

$$\Sigma_{\text{melt}} \equiv C_{\text{melt}} \left(\theta_{\text{cavity}} - \theta^{\text{f}}_{\text{cavity}} \right). \tag{8}$$

Here $\theta^{\text{f}}_{\text{cavity}}$ is the melt-weighted freezing temperature at the base of the FRIS; it is implicit in (8) that the net melt approaches zero as θ_{cavity} approaches $\theta^{\text{f}}_{\text{cavity}}$. In Fig. 10(b) we test this relationship and estimate the linear coefficient C_{melt}. We find that linear fits to the model experiments simulating a warm FRIS state and a cold FRIS state explain almost all of the vari-

Table 2: Constants used in our conceptual model solutions. The thermal expansion coefficient α and haline contraction coefficient β are calculated using the Gibbs Seawater Oceanographic toolbox (McDougall & Barker, 2011) assuming a depth of 300m, a temperature that is the average of θ_{mWDW} and θ_{HSSW}, and a reference salinity of 34 psu.

Parameter	Description	Value
C_{polynya}	Polynya salt flux/wind perturbation coefficient	$5.5\times10^{8}\,\mathrm{g/s}$
C_{melt}	Melt rate/cavity temperature coefficient	$8.1\times10^{8}\,\mathrm{g/s^{\circ}C}$
$\Sigma^{0}_{\mathrm{polynya}}$	Polynya salt flux offset	$-2.0\times10^{8}\,\mathrm{g/s}$
f_{melt}	Fraction of meltwater mixing with HSSW	0.3
α	Thermal expansion coefficient	$3\times10^{-5}\,\mathrm{K^{-1}}$
β	Haline contraction coefficient	$8\times10^{-4}\,\mathrm{psu^{-1}}$
Ψ	Rate of transformation from AASW to HSSW	1.3 Sv
ρ_0	Reference density	$1000\,\mathrm{kg/m^3}$
S_{AASW}	Salinity of AASW	34.25 psu
S_{mWDW}	Salinity of mWDW	34.35 psu
θ_{mWDW}	Potential temperature of mWDW	-1°C
θ_{HSSW}	Potential temperature of HSSW	-2.1°C
$\theta^{\mathrm{f}}_{\mathrm{cavity}}$	Melt-weighted cavity freezing temperature	-2.3°C

ance in the relationships between Σ_{melt} and $\theta_{\mathrm{cavity}}-\theta^{\mathrm{f}}_{\mathrm{cavity}}$. Based on this, we select a value of $C_{\mathrm{melt}}=8.1\times10^{8}\,\mathrm{g/s^{\circ}C}$ for our conceptual model.

The combination of equations (4)—(8) implies that S_{HSSW} is effectively a function of χ and θ_{cavity}. To obtain solutions to our conceptual model, we evaluate the density difference between HSSW and WDW at the ice shelf front as

$$\sigma_{\mathrm{HSSW}}-\sigma_{\mathrm{mWDW}}\approx\rho_0\left\{\beta\left[S_{\mathrm{HSSW}}(\chi,\theta_{\mathrm{cavity}})-S_{\mathrm{mWDW}}\right]-\alpha\left[\theta_{\mathrm{HSSW}}-\theta_{\mathrm{mWDW}}\right]\right\}. \tag{9}$$

Here we have used a local linear approximation to the model's full, nonlinear equation of state (Jackett & Mcdougall, 1995) for analytical simplicity, where β is the haline contraction coefficient and α is the thermal expansion coefficient. We have explicitly written the dependence of S_{HSSW} on χ and θ_{cavity} for conceptual clarity. Equation (3) states that for a given value of χ there are two possible solutions: (i) mWDW floods the cavity, implying that $\theta_{\mathrm{cavity}}=\theta_{\mathrm{mWDW}}$ and requiring that the right-hand side of (9) is less than zero; (ii) HSSW floods the cavity, implying that $\theta_{\mathrm{cavity}}=\theta_{\mathrm{HSSW}}$ and requiring that the right-hand side of (9) is greater than zero. Depending on the value of χ, we find that one or both of the requirements of (i) and (ii) may be met; if both are satisfied for a given value of χ then there exist both "warm" and "cold" FRIS cavity equilibria for the same meridional winds. A complete analytical solution of (3)–(9) is provided in the Supporting Information.

In Fig. 11 we compare the cavity temperature, cavity salinity and cavity-integrated melt rates drawn from our conceptual model against those diagnosed from our meridional wind perturbation experiments. Values used for the constants in (3)–(9) are listed in Table 2. Panel (a) compares the selected values of θ_{mWDW} and θ_{HSSW} against the values of θ_{cavity} diagnosed from the warm-state and cold-state experiments, respectively, over the range of χ for which we find bi-stability. Panel (b) similarly compares the selected value of S_{mWDW} with the diagnosed values of S_{cavity} in the warm-state experiments. In panel (b) we also compare the predicted values of S_{HSSW} given by (4)–(8) with the diagnosed values of S_{cavity} from the cold-state experiments. Finally, in panel (c) we compare the melt rates given by the conceptual model via equation (8) for the warm and cold FRIS states against the melt rates diagnosed from our merid-

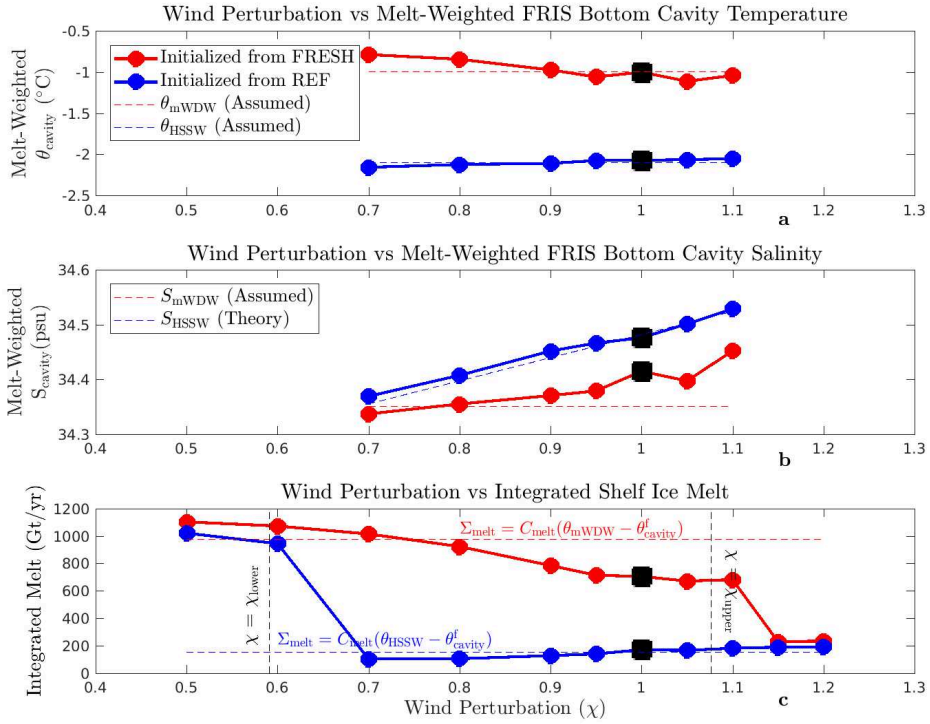

Figure 11: Comparison of Filchner-Ronne Ice Shelf (FRIS) cavity properties between our conceptual model and our meridional wind perturbation experiments, as functions of the dimensionless meridional wind perturbation, χ. (a) Melt-weighted cavity bottom temperatures, θ_{cavity}, over the range of χ for which the simulations are bistable, compared with the selected values of θ_{mWDW} and θ_{HSSW} used in our conceptual model. (b) Melt-weighted cavity bottom salinity, S_{cavity}, over the range of χ for which the simulations are bistable, compared with the selected value of S_{mWDW} and with the values of S_{HSSW} predicted by (4). (c) Area-integrated Filchner-Ronne Ice Shelf (FRIS) melt rates, compared with melt rates from our conceptual model (8) using $\theta_{\text{cavity}} = \theta_{\text{mWDW}}$ (red dashed line) and $\theta_{\text{cavity}} = \theta_{\text{HSSW}}$ (blue dashed line). Black dashed lines indicate the theoretical bounds on the range of wind stress perturbation χ for which the FRIS is bistable, obtained by solving our conceptual model equations (4)–(9). All quantities are averaged over the last full 9-year atmospheric forcing cycle in each simulation. Black squares indicate the REF and FRESH experiments, discussed in §3. Red and blue dots indicate simulations initialized with the FRIS cavity in a warm and cold states (from the FRESH and REF simulations), respectively.

ional wind perturbation experiments. We additionally solve (3)–(9) to determine the range of wind stress perturbations, $\chi_{\text{lower}} < \chi < \chi_{\text{upper}}$, over which the FRIS cavity should be bistable. Our conceptual model predicts that the bounds of this range should be $\chi_{\text{lower}} = 0.59$ and $\chi_{\text{upper}} = 1.08$. These fall close to the diagnosed bounds of the hysteresis loop, which lie between 0.6–0.7 and 1.1–1.15, respectively. Thus, our conceptual model qualitatively reproduces the hysteresis found in our meridional wind perturbation experiments.

5 Discussion and Conclusions

In this study, we developed a regional model of the Weddell Sea (see §2.1) to explore the sensitivity of the Filchner-Ronne Ice Shelf (FRIS) cavity circulation to local atmospheric

forcing. In §2.2 we showed that the Weddell Sea Regional Model (WSRM) qualitatively reproduces the observed state and circulation of the southern Weddell Sea and FRIS cavity (Nicholls et al., 2009). In §3.1 we found that the sensitivity of the FRIS cavity circulation is complicated by a bi-stability: the FRIS approaches either a relatively "cold" cavity with melt rates comparable to those observed (Moholdt et al., 2014), or a relatively "warm" cavity with melt rates an order of magnitude higher, depending on the model's initial conditions in the FRIS cavity (Figs. 3–5). This is consistent with the findings of Hellmer et al. (2017), who found the access of mWDW to the Filchner Trough was controlled by the bottom salinity (and thus bottom density) in global simulations forced by 21st Century atmospheric forcing projections. In our experiments, mWDW similarly only enters the Filchner Trough (not shown), and thus the FRIS cavity, in the "cold-state" experiments.

Because the transition between stable states corresponds to a dramatic change in the FRIS cavity melt rate, we chose to focus our analysis on the capacity of atmospheric forcing perturbations to "switch" between FRIS states. In §3.2 we tested this by imposing perturbations to the zonal winds, meridional winds and atmospheric surface temperature over the entire WSRM domain. We found that relatively modest (20–50%) perturbations to the meridional winds were sufficient to switch the FRIS cavity between its warm and cold states, whereas relatively extreme perturbations to the zonal winds and atmospheric temperature did not (see Fig. 6). In §4.1 we therefore performed a suite of meridional wind perturbation experiments to map out a hysteresis loop (Fig. 7). These experiments indicate that the FRIS cavity is bi-stable between a 30% weakening and a 10% strengthening of the reference meridional winds. Within this range, the FRIS cavity circulation, melt rate, and water mass properties are dependent on the initial cavity stratification.

Our experiments suggest that the "warm" and "cold" FRIS cavity states correspond to the cavity being flooded by one of two different water masses: modified Warm Deep Water (mWDW) and High-Salinity Shelf Water (HSSW), respectively (Nicholls et al., 2009). This motivated us to develop a conceptual model, described in §4.2, to explain the bi-stability of the FRIS cavity (see Fig. 9). We posited that the cavity is occupied by either mWDW or HSSW, depending on which is denser, and that the salinity of HSSW in particular is key to determining this density difference. Crucially, salinity of HSSW depends upon the rate of salt input in the Ronne polynya, which is linearly proportional to the strength of the local meridional winds, and upon the volume of meltwater produced under the FRIS, which approximately increases linearly with the potential temperature of the densest waters in the cavity (see Fig. 10). This model yields bi-stable solutions over a similar range of the meridional wind perturbation parameter χ as our WSRM simulations.

Taken together, our results suggest that the bi-stability can be understood via the following thought experiment: if we start from a "cold" FRIS state with HSSW flooding the cavity ($\chi = 1$ in our model), as currently observed in nature, and continuously reduce the strength of the meridional winds, then the salinity and density of newly-formed HSSW will decrease commensurately. For sufficiently weak winds ($\chi < \chi_{\text{lower}}$ in our model), the density of HSSW becomes lower than that of mWDW, at which point mWDW will flood the cavity instead, increasing the FRIS basal melt rate by an order of magnitude. This leads to a positive feedback: the increased production of meltwater further reduces the salinity and density of HSSW (Hellmer et al., 2017). If we then increase the meridional winds again, HSSW will experience a commensurate increase in its salinity and density. However, the freshening effect of the increased meltwater output means that the winds must exceed a much higher threshold ($\chi > \chi_{\text{upper}}$ in our model) to create HSSW with a greater density than mWDW. Thus there exists a hysteresis: for a range of meridional wind strengths ($\chi_{\text{lower}} < \chi < \chi_{\text{upper}}$ in our model), the state of the FRIS' circulation and melt rate depends not only on the strength of the meridional winds, but also on its own time-history.

Though this study highlights a potentially important mechanism for "switching" the mode of melting in the FRIS (Jacobs et al., 1992; Dinniman et al., 2016), our approach carries several caveats. While the WSRM model state compares well to observations, there are some bi-

ases that exist in the sea ice state, the strength of the ASF, and the properties of HSSW. The anomalously fresh HSSW, in particular, may make the model cavity more susceptible to a switch over to the "warm" state, and may also influence the density gradients and circulation within the FRIS cavity. These biases may be ameliorated by future work to refine the WSRM's horizontal grid (Newsom et al., 2016; Dufour et al., 2017), which would also be required to adequately resolve the effects of mesoscale eddies (St-Laurent et al., 2013; A. L. Stewart & Thompson, 2015a) and tides (Mueller et al., 2018; A. L. Stewart et al., 2018, 2019). However, we do not expect higher-resolution simulations to yield qualitatively different findings from those reported here. Other shortcomings of the regional model setup include the model's 9-year atmospheric forcing cycle, which captures limited interannual variability and no variability on decadal timescales and longer. The use of constant turbulent transfer velocity for heat and freshwater across the ice shelf-ocean boundary layer omits important feedbacks between the cavity circulation and the melt rate (Jourdain et al., 2017), and suppresses tidal enhancement of basal melt rates (Mueller et al., 2018).

Another caveat is that although the atmospheric forcing perturbation experiments in §3.2 suggest that offshore winds most efficiently "switch" the cavity between its warm and cold states, we have not performed an exhaustive search. Indeed, it would almost certainly be possible to enforce a switch in the cavity state via other perturbations, for example by warming the surface air temperature to the point that no sea ice can grow. Motivated by simplicity in our experimental design, we applied our wind perturbation uniformly across the model domain, which has the side effects of modifying both the coastal and open-ocean winds, and of changing the direction of the winds (Mathiot et al., 2010). However, the diagnosed and conceptually modeled changes in HSSW production in §4 suggest that qualitatively similar results would be obtained if only the katabatic winds near the front of the FRIS were modified. We have also not discussed perturbations to the ocean state, which are anticipated to be particularly impactful if made upstream (*i.e.* east) of the Weddell Sea (Thoma et al., 2006; Graham et al., 2013). Preliminary experiments with modifying the depth of the Antarctic Slope Front (ASF) at the eastern boundary did not lead to substantial changes in the FRIS cavity and so were not pursued further in this study. However, again, perturbations to the offshore stratification could almost certainly be contrived to switch between cavity states, for example via a glacial period-like cooling of WDW to the surface freezing temperature (Miller et al., 2012; Adkins, 2013) to prevent the FRIS experiencing the elevated melt rates diagnosed in the "warm" state.

In this study we focused on the transition between "warm" and "cold" FRIS states, but our meridional wind perturbation experiments indicate that the melt rate still varies by a factor of $\sim$2 if one considers only experiments that equilibrate to a warm state, or only experiments that equilibrate to a cold state (see Fig. 7). A plausible explanation for the increase in the cold-state FRIS melt rate with the strength of the meridional winds is an increased rate of HSSW circulation (Ψ) through the cavity, driven by the higher density of HSSW (Grosfeld et al., 1997; Grosfeld & Gerdes, 1998). Similarly, a plausible explanation for the decrease in the warm-state FRIS melt rate with the strength of the meridional winds is that WDW becomes more strongly modified, and therefore enters the cavity at a lower potential temperature. Such hypotheses for the diagnosed, order-one variations in the cavity state, circulation and melt rate remain to be tested. These effects are also not accounted for in our conceptual model, which makes various severe simplifications of the dynamics and contains choices of the values for certain constants remain somewhat arbitrary. A more complete theory for the circulation within the FRIS and other ice shelf cavities should explicitly represent the process of WDW modification, the strength and pathways of the buoyancy-driven cavity circulation, the onshore transport of WDW from the continental shelf break, and the fraction of the FRIS cavity-sourced meltwater that mixes with HSSW on the continental shelf. In its current form, our conceptual model serves primarily to illustrate the fundamental mechanism underlying the bi-stability of the FRIS, and has much scope for future development and refinement.

In summary, our findings indicate that the FRIS cavity is bi-stable, and that shifts between stable states can be mediated by changes in the local katabatic winds via their influence

on the salinity of HSSW. This has implications for the future of the FRIS and potentially many other ice shelves around Antarctica, as there is no element of the proposed mechanism that is unique to the FRIS. One implication is that because HSSW that currently enters the FRIS cavity is somewhat denser than that simulated by the WSRM (see §2), the cavity may be buffered against mWDW intrusions in coming decades (Nicholls et al., 2009; Darelius et al., 2016). Our results may also offer insight as to why these mWDW intrusions have been predicted to occur in some model projections (Hellmer et al., 2012, 2017), but not in others (Timmermann & Hellmer, 2013; Naughten et al., 2018). In contrast, other ice shelves associated with weaker katabatic winds and less dense shelf waters may be more vulnerable to changes in the mWDW/mCDW reservoir on the continental shelf, to local atmospheric conditions, or to melt rates of adjacent ice shelves (Silvano et al., 2018). Our results therefore motivate further evaluation of ongoing and potential future changes in the katabatic winds (Hazel & Stewart, 2019; Bintanja et al., 2014). Further process-oriented simulations will likely be required to provide a more general characterization of ice shelf cavities' dependence on local and global atmospheric/oceanic changes (Grosfeld et al., 1997; Grosfeld & Gerdes, 1998), as mediated by mesoscale/submesoscale eddy transports (Årthun et al., 2013; A. L. Stewart & Thompson, 2015b; A. L. Stewart, 2019), tidally-induced transport (Mueller et al., 2018), and the geometry of the cavity itself (de Rydt et al., 2014; Zhao et al., 2019).

Acknowledgments

All new data presented in this study are output from model simulations using the publicly-available Massachusetts Institute of Technology general circulation model (MITgcm), which is available via `http://mitgcm.org/`. Matlab scripts used to generate, run, and analyze these simulations are available via `https://doi.org/10.5281/zenodo.3529796`. This material is based in part upon work supported by the National Science Foundation under Grant Numbers ANT-1543388, and OCE-1751386, and by the National Aeronautics and Space Administration ROSES Physical Oceanography program under grant number 80NSSC19K1192. This work used the Extreme Science and Engineering Discovery Environment (XSEDE, Towns et al. (2014)), which is supported by National Science Foundation grant number ACI-1548562. The authors thank Tiago Dotto and Tore Hattermann for sharing available observational datasets used for model evaluation purposes. The authors additionally thank Andy Thompson, Jim McWilliams and Marcelo Chamecki for various discussions that improved this study. Finally, the authors thank Hartmut Hellmer and an anonymous reviewer for many constructive comments that substantially improved the manuscript.

References

Adcroft, A., Campin, J.-M., Doddridge, E., Dutkiewicz, S., Evangelinos, C., Ferreira, D., ... Scott, J. (2018). *Mitgcm documentation* (Vol. 19; Tech. Rep.).

Adkins, J. F. (2013). The role of deep ocean circulation in setting glacial climates. *Paleoceanography*, *28*(3), 539–561.

Armitage, T. K., Kwok, R., Thompson, A. F., & Cunningham, G. (2018). Dynamic topography and sea level anomalies of the Southern Ocean: Variability and teleconnections. *Journal of Geophysical Research: Oceans*, *123*(1), 613–630.

Årthun, M., Holland, P. R., Nicholls, K. W., & Feltham, D. L. (2013). Eddy-driven exchange between the open ocean and a sub–ice shelf cavity. *J. Phys. Oceanogr.*, *43*(11), 2372–2387.

Bintanja, R., Severijns, C., Haarsma, R., & Hazeleger, W. (2014). The future of Antarctica's surface winds simulated by a high-resolution global climate model: 2. Drivers of 21st century changes. *J. Geophys. Res. Atmospheres*, *119*(12), 7160–7178.

Cole, S. T., Timmermans, M.-L., Toole, J. M., Krishfield, R. A., & Thwaites, F. T. (2014). Ekman veering, internal waves, and turbulence observed under arctic sea ice. *Journal of Physical Oceanography*, *44*(5), 1306–1328.

Comiso, J. C., & Gordon, A. L. (1998). Interannual variability in summer sea ice minimum,

coastal. *Antarctic Research Series*, *74*, 293–315.

Daae, K., Hattermann, T., Darelius, E., & Fer, I. (2017). On the effect of topography and wind on warm water inflow: An idealized study of the southern Weddell Sea continental shelf system. *Journal of Geophysical Research: Oceans*.

Darelius, E., Fer, I., & Nicholls, K. W. (2016). Observed vulnerability of Filchner-Ronne Ice Shelf to wind-driven inflow of warm deep water. *Nature communications*, *7*, 12300.

Darelius, E., & Sallee, J.-B. (2018). Seasonal outflow of ice shelf water across the front of the Filchner ice shelf, Weddell Sea, Antarctica. *Geophysical Research Letters*, *45*(8), 3577–3585.

de Rydt, J., Holland, P. R., Dutrieux, P., & Jenkins, A. (2014). Geometric and oceanographic controls on melting beneath Pine Island Glacier. *Journal of Geophysical Research: Oceans*, *119*(4), 2420–2438.

Dinniman, M. S., Asay-Davis, X. S., Galton-Fenzi, B. K., Holland, P. R., Jenkins, A., & Timmermann, R. (2016). Modeling ice shelf/ocean interaction in Antarctica: A review. *Oceanography*, *29*(4), 144–153.

Dufour, C. O., Morrison, A. K., Griffies, S. M., Frenger, I., Zanowski, H., & Winton, M. (2017). Preconditioning of the Weddell Sea polynya by the ocean mesoscale and dense water overflows. *J. Climate*, *30*(19), 7719–7737.

Foldvik, A., Gammelsrød, T., Østerhus, S., Fahrbach, E., Rohardt, G., Schröder, M., ... Woodgate, R. (2004). Ice shelf water overflow and bottom water formation in the southern Weddell Sea. *Journal of Geophysical Research: Oceans*, *109*(C2).

Fox, A. J., Paul, A., & Cooper, R. (1994). Measured properties of the Antarctic ice sheet derived from the SCAR Antarctic digital database. *Polar Record*, *30*(174), 201–206.

Gade, H. G. (1979). Melting of ice in sea water: A primitive model with application to the Antarctic ice shelf and icebergs. *Journal of Physical Oceanography*, *9*(1), 189–198.

Gerdes, R., Determann, J., & Grosfeld, K. (1999). Ocean circulation beneath Filchner-Ronne Ice Shelf from three-dimensional model results. *J. Geophys. Res. Oceans*, *104*(C7), 15827–15842.

Gordon, A. L., Huber, B., McKee, D., & Visbeck, M. (2010). A seasonal cycle in the export of bottom water from the Weddell Sea. *Nat. Geosci.*, *3*(8), 551.

Graham, J. A., Heywood, K. J., Chavanne, C. P., & Holland, P. R. (2013). Seasonal variability of water masses and transport on the Antarctic continental shelf and slope in the southeastern Weddell Sea. *Journal of Geophysical Research: Oceans*, *118*(4), 2201–2214.

Grosfeld, K., & Gerdes, R. (1998). Circulation beneath the Filchner Ice Shelf, Antarctica, and its sensitivity to changes in the oceanic environment: a case-study. *Ann. Glaciol.*, *27*, 99–104.

Grosfeld, K., Gerdes, R., & Determann, J. (1997). Thermohaline circulation and interaction between ice shelf cavities and the adjacent open ocean. *J. Geophys. Res. Oceans*, *102*(C7), 15595–15610.

Grosfeld, K., Schröder, M., Fahrbach, E., Gerdes, R., & Mackensen, A. (2001). How iceberg calving and grounding change the circulation and hydrography in the Filchner Ice Shelf-Ocean System. *J. Geophys. Res. Oceans*, *106*(C5), 9039–9055.

Haid, V., & Timmermann, R. (2013). Simulated heat flux and sea ice production at coastal polynyas in the southwestern Weddell Sea. *Journal of Geophysical Research: Oceans*, *118*(5), 2640–2652.

Hattermann, T. (2018). Antarctic Thermocline Dynamics along a Narrow Shelf with Easterly Winds. *Journal of Physical Oceanography*, *48*(10), 2419–2443.

Hattermann, T., & Rohardt, G. (2018). *Kapp Norvegia Antarctic Slope Front climatology* [data set]. PANGAEA. Retrieved from `https://doi.org/10.1594/PANGAEA.893199` (Supplement to: Hattermann, Tore (2018): Antarctic Thermocline Dynamics along a Narrow Shelf with Easterly Winds. Journal of Physical Oceanography, 48(10), 2419-2443, https://doi.org/10.1175/JPO-D-18-0064.1) doi: 10.1594/PANGAEA.893199

Hattermann, T., Smedsrud, L. H., Nøst, O. A., Lilly, J. M., & Galton-Fenzi, B. K. (2014).

Eddy-Resolving Simulations of the Fimbul Ice Shelf Cavity Circulation: Basal Melting and Exchange with the Open Ocean. *Ocean Modelling*, *82*, 28–44.

Hazel, J. E. (2019). *Exploring the Wind-Driven Near-Antarctic Circulation.* (Doctoral dissertation, UCLA). Retrieved from `https://escholarship.org/uc/item/1gs7z5zm`

Hazel, J. E., & Stewart, A. L. (2019). Are the Near-Antarctic Easterly Winds Weakening in Response to Enhancement of the Southern Annular Mode? *Journal of Climate*, *32*(6), 1895–1918.

Hellmer, H. H., Kauker, F., Timmermann, R., Determann, J., & Rae, J. (2012). Twenty-First-Century Warming of a Large Antarctic Ice-Shelf Cavity by a Redirected Coastal Current. *Nature*, *485*(7397), 225–228.

Hellmer, H. H., Kauker, F., Timmermann, R., & Hattermann, T. (2017). The fate of the southern Weddell Sea continental shelf in a warming climate. *Journal of Climate*, *30*(12), 4337–4350.

Hibler III, W. D. (1979). A dynamic thermodynamic sea ice model. *Journal of Physical Oceanography*, *9*(4), 815–846.

Jackett, D. R., & Mcdougall, T. J. (1995). Minimal adjustment of hydrographic profiles to achieve static stability. *Journal of Atmospheric and Oceanic Technology*, *12*(2), 381–389.

Jacobs, S. S. (1991). On the Nature and Significance of the Antarctic Slope Front. *Marine Chemistry*, *35*(1), 9–24.

Jacobs, S. S., Helmer, H. H., Doake, C. S. M., Jenkins, A., & Frolich, R. M. (1992). Melting of ice shelves and the mass balance of Antarctica. *J. Glaciol.*, *38*(130), 375–387.

Jenkins, A., Hellmer, H. H., & Holland, D. M. (2001). The Role of Meltwater Advection in the formulation of conservative boundary conditions at an ice–ocean interface. *Journal of physical oceanography*, *31*(1), 285–296.

Jenkins, A., & Holland, D. M. (2002). A model study of ocean circulation beneath Filchner-Ronne Ice Shelf, Antarctica: Implications for bottom water formation. *Geophys. Res. Lett.*, *29*(8), 34–1.

Jourdain, N. C., Mathiot, P., Merino, N., Durand, G., Le Sommer, J., Spence, P., … Madec, G. (2017). Ocean circulation and sea-ice thinning induced by melting ice shelves in the Amundsen Sea. *J. Geophys. Res. Oceans*, *122*(3), 2550–2573.

Jullion, L., Naviera Garabato, A. C., Bacon, S., Meredith, M. P., Brown, P. J., Torres-Valdés, S., … others (2014). The contribution of the Weddell Gyre to the lower limb of the Global Overturning Circulation. *J. Geophys. Res. Oceans*, *119*(6), 3357–3377.

Klinck, J., & Dinniman, M. (2010). Exchange across the shelf break at high southern latitudes. *Ocean Science*, *6*(2).

Large, W. G., McWilliams, J. C., & Doney, S. C. (1994). Oceanic vertical mixing: A review and a model with a nonlocal boundary layer parameterization. *Reviews of Geophysics*, *32*(4), 363–403.

Lavergne, T., Sørensen, A. M., Kern, S., Tonboe, R., Notz, D., Aaboe, S., … others (2019). Version 2 of the EUMETSAT OSI SAF and ESA CCI sea-ice concentration climate data records. *Cryosphere*, *13*(1), 49–78.

Leppäranta, M. (2011). *The drift of sea ice*. Springer Science & Business Media.

Losch, M. (2008). Modeling ice shelf cavities in a z coordinate ocean general circulation model. *Journal of Geophysical Research: Oceans*, *113*(C8).

Losch, M., Menemenlis, D., Campin, J.-M., Heimbach, P., & Hill, C. (2010). On the formulation of sea-ice models. Part 1: Effects of different solver implementations and parameterizations. *Ocean Modell.*, *33*(1-2), 129–144.

Marshall, J., Adcroft, A., Hill, C., Perelman, L., & Heisey, C. (1997). A finite-volume, incompressible Navier Stokes model for studies of the ocean on parallel computers. *Journal of Geophysical Research: Oceans*, *102*(C3), 5753–5766.

Marshall, J., Hill, C., Perelman, L., & Adcroft, A. (1997). Hydrostatic, quasi-hydrostatic, and nonhydrostatic ocean modeling. *Journal of Geophysical Research: Oceans*, *102*(C3), 5733–5752.

Mathiot, P., Barnier, B., Gallée, H., Molines, J. M., Le Sommer, J., Juza, M., & Penduff, T.

(2010). Introducing katabatic winds in global ERA40 fields to simulate their impacts on the Southern Ocean and sea-ice. *Ocean Modell.*, *35*(3), 146–160.

Mazloff, M. R., Heimbach, P., & Wunsch, C. (2010). An eddy-permitting Southern Ocean state estimate. *Journal of Physical Oceanography*, *40*(5), 880–899.

McDougall, T. J., & Barker, P. M. (2011). Getting started with TEOS-10 and the Gibbs Seawater (GSW) oceanographic toolbox. *SCOR/IAPSO WG*, *127*, 1–28.

Miller, M. D., Adkins, J. F., Menemenlis, D., & Schodlok, M. P. (2012). The role of ocean cooling in setting glacial southern source bottom water salinity. *Paleoceanography*, *27*(3).

Moholdt, G., Padman, L., & Fricker, H. A. (2014). Basal mass budget of Ross and Filchner-Ronne ice shelves, Antarctica, derived from Lagrangian analysis of ICESat altimetry. *Journal of Geophysical Research: Earth Surface*, *119*(11), 2361–2380.

Mueller, R. D., Hattermann, T., Howard, S. L., & Padman, L. (2018). Tidal influences on a future evolution of the Filchner–Ronne Ice Shelf cavity in the Weddell Sea, Antarctica. *Cryosphere*, *12*(2), 453–476.

Naughten, K. A., Meissner, K. J., Galton-Fenzi, B. K., England, M. H., Timmermann, R., & Hellmer, H. H. (2018). Future projections of Antarctic ice shelf melting based on CMIP5 scenarios. *J. Climate*, *31*(13), 5243–5261.

Newsom, E. R., Bitz, C. M., Bryan, F. O., Abernathey, R., & Gent, P. R. (2016). Southern Ocean deep circulation and heat uptake in a high-resolution climate model. *Journal of Climate*, *29*(7), 2597–2619.

Nicholls, K., Østerhus, S., Makinson, K., Gammelsrød, T., & Fahrbach, E. (2009). Ice-ocean processes over the continental shelf of the southern Weddell Sea, Antarctica: A review. *Reviews of Geophysics*, *47*(3).

Nøst, O. A., Biuw, M., Tverberg, V., Lydersen, C., Hattermann, T., Zhou, Q., ... Kovacs, K. M. (2011). Eddy overturning of the Antarctic Slope Front controls glacial melting in the Eastern Weddell Sea. *Journal of Geophysical Research: Oceans*, *116*(C11).

Padman, L., Fricker, H. A., Coleman, R., Howard, S., & Erofeeva, L. (2002). A new tide model for the Antarctic ice shelves and seas. *Annals of Glaciology*, *34*(1), 247–254.

Park, H.-S., & Stewart, A. L. (2016). An analytical model for wind-driven arctic summer sea ice drift. *The Cryosphere*, *10*(1), 227–244.

Petrich, C., & Eicken, H. (2017). Overview of sea ice growth and properties. *Sea ice*, 1–41.

Powers, J. G., Manning, K. W., Bromwich, D. H., Cassano, J. J., & Cayette, A. M. (2012). A decade of antarctic science support through amps. *Bulletin of the American Meteorological Society*, *93*(11), 1699–1712.

Rignot, E., Jacobs, S., Mouginot, J., & Scheuchl, B. (2013). Ice-shelf melting around Antarctica. *Science*, *341*(6143), 266–270.

Rocha, C. B., Chereskin, T. K., Gille, S. T., & Menemenlis, D. (2016). Mesoscale to submesoscale wavenumber spectra in Drake Passage. *Journal of Physical Oceanography*, *46*(2), 601–620.

Schmidt, G. A., Bitz, C. M., Mikolajewicz, U., & Tremblay, B. L. (2004). Ice–ocean boundary conditions for coupled models. *Ocean Modelling*, *7*(1-2), 59–74.

Silvano, A., Rintoul, S. R., Peña-Molino, B., Hobbs, W. R., van Wijk, E., Aoki, S., ... Williams, G. D. (2018). Freshening by glacial meltwater enhances melting of ice shelves and reduces formation of Antarctic Bottom Water. *Sci. Adv.*, *4*(4), eaap9467.

Smith, S. D., Muench, R. D., & Pease, C. H. (1990). Polynyas and leads: An overview of physical processes and environment. *Journal of Geophysical Research: Oceans*, *95*(C6), 9461–9479.

Stewart, A. L. (2019). Approximating Isoneutral Ocean Transport via the Temporal Residual Mean. *Fluids*, *4*(4), 179.

Stewart, A. L., Klocker, A., & Menemenlis, D. (2018). Circum-Antarctic shoreward heat transport derived from an eddy-and tide-resolving simulation. *Geophysical Research Letters*, *45*(2), 834–845.

Stewart, A. L., Klocker, A., & Menemenlis, D. (2019). Acceleration and overturning of the Antarctic Slope Current by winds, eddies, and tides. *J. Phys. Oceanogr.*, *49*(8), 2043–

2074.

Stewart, A. L., & Thompson, A. F. (2012). Sensitivity of the ocean's deep overturning circulation to easterly Antarctic winds. *Geophysical Research Letters*, *39*(18).

Stewart, A. L., & Thompson, A. F. (2013). Connecting Antarctic cross-slope exchange with Southern Ocean overturning. *Journal of Physical Oceanography*, *43*(7), 1453–1471.

Stewart, A. L., & Thompson, A. F. (2015a). Eddy-mediated transport of warm Circumpolar Deep Water across the Antarctic shelf break. *Geophysical Research Letters*, *42*(2), 432–440.

Stewart, A. L., & Thompson, A. F. (2015b). The neutral density temporal residual mean overturning circulation. *Ocean Modell.*, *90*, 44–56.

Stewart, K., Hogg, A. M., Griffies, S., Heerdegen, A., Ward, M., Spence, P., & England, M. (2017). Vertical resolution of baroclinic modes in global ocean models. *Ocean Modelling*, *113*, 50–65.

St-Laurent, P., Klinck, J. M., & Dinniman, M. S. (2013). On the role of coastal troughs in the circulation of warm Circumpolar Deep Water on Antarctic shelves. *Journal of Physical Oceanography*, *43*(1), 51–64.

Tamura, T., Ohshima, K. I., Fraser, A. D., & Williams, G. D. (2016). Sea ice production variability in Antarctic coastal polynyas. *J. Geophys. Res. Oceans*, *121*(5), 2967–2979.

Tamura, T., Ohshima, K. I., & Nihashi, S. (2008). Mapping of sea ice production for Antarctic coastal polynyas. *Geophys. Res. Lett.*, *35*(7).

Thoma, M., Determann, J., Grosfeld, K., Goeller, S., & Hellmer, H. H. (2015). Future sea-level rise due to projected ocean warming beneath the Filchner Ronne Ice Shelf: A coupled model study. *Earth Planet. Sci. Lett.*, *431*, 217–224.

Thoma, M., Grosfeld, K., & Lange, M. A. (2006). Impact of the Eastern Weddell Ice Shelves on water masses in the eastern Weddell Sea. *J. Geophys. Res. Oceans*, *111*(C12).

Thorndike, A. S., & Colony, R. (1982). Sea ice motion in response to geostrophic winds. *Journal of Geophysical Research: Oceans*, *87*(C8), 5845–5852.

Timmermann, R. (2010). RTOPO-1: A consistent dataset for Antarctic ice shelf topography and global ocean bathymetry. In *EGU General Assembly Conference Abstracts* (Vol. 12, p. 5304).

Timmermann, R., & Hellmer, H. H. (2013). Southern Ocean warming and increased ice shelf basal melting in the twenty-first and twenty-second centuries based on coupled ice-ocean finite-element modelling. *Ocean Dynam.*, *63*(9-10), 1011–1026.

Towns, J., Cockerill, T., Dahan, M., Foster, I., Gaither, K., Grimshaw, A., ... Wilkins-Diehr, N. (2014, Sept). XSEDE: Accelerating scientific discovery. *Computing in Science Engineering*, *16*(5), 62-74. doi: 10.1109/MCSE.2014.80

Vernet, M., Geibert, W., Hoppema, M., Brown, P. J., Haas, C., Hellmer, H. H., ... others (2019). The weddell gyre, southern ocean: present knowledge and future challenges. *Rev. Geophys.*, *57*, 623–708.

Wang, Q., Danilov, S., Hellmer, H., Sidorenko, D., Schroeter, J., & Jung, T. (2013). Enhanced cross-shelf exchange by tides in the western Ross Sea. *Geophysical Research Letters*, *40*(21), 5735–5739.

Zhang, J., & Hibler III, W. D. (1997). On an efficient numerical method for modeling sea ice dynamics. *Journal of Geophysical Research: Oceans*, *102*(C4), 8691–8702.

Zhao, K. X., Stewart, A. L., & McWilliams, J. C. (2019). Sill-Influenced Exchange Flows in Ice Shelf Cavities. *J. Phys. Oceanogr.*, *49*(1), 163–191.